Remote Sensing of Environment 330 (2025) 114996

Contents lists available at ScienceDirect

Remote Sensing of Environment

journal homepage: www.elsevier.com/locate/rse

Spatial patterns of leaf angle distribution covary with canopy fluorescence yield, reflectance indices, and leaf chlorophyll content, in a mixed temperate forest☆

Andrew D. Jablonski *, Rong Li, Jongmin Kim, Manuel Lerdau, Carmen Petras, Xi Yang *

Department of Environmental Sciences, University of Virginia, Charlottesville, Virginia, USA

ARTICLE INFO

Keywords:
Solar-induced chlorophyll fluorescence (SIF)
Terrestrial laser scanning (TLS)
Leaf angle distribution
Near-infrared radiance of vegetation
Normalized difference vegetation index (NDVI)
Fluorescence yield
Plant canopy

ABSTRACT

Plant canopies are integrated units that coordinate their functional (e.g., foliar biochemistry) and structural properties. This coordination affects remote sensing observations of canopy reflectance and solar-induced chlorophyll fluorescence (SIF). One key canopy structural property is leaf angle. Despite the fact that radiative transfer models have shown the crucial role of leaf angle in modulating remote sensing signals, methodological and technological barriers have prevented detailed investigations of how leaf angle covaries with canopy function and remote sensing observations. In this study, we employ a novel uncrewed aerial system (UAS) called FluoSpecAir to study the spatial patterns in far-red (FR) SIF ($SIF_{obs,FR}$), near-infrared reflectance and radiance of vegetation (NIR_V and NIR_VR), normalized difference vegetation index (NDVI), and chlorophyll:carotenoid index (CCI), across individual tree canopies during two separate time periods. Additionally, we collected 3D scans of individual tree canopies using terrestrial laser scanning (TLS) and estimated foliar pigment content from leaf reflectance spectra. We used the 3D scans to calculate the leaf angle distribution (LAD) and leaf area voxel density (LAVD) of each canopy. We modeled LAD using a beta distribution, which is parameterized by μ and ν, and the leaf inclination distribution function (LIDF), which is parameterized by LIDFa and LIDFb. We found that ν and μ, which are inversely related to the variance in leaf angle, covaried with spatial patterns in peak growing season canopy CCI, NDVI, $SIF_{obs,FR}$, and $\frac{SIF_{obs,FR}}{NIR_VR}$, and leaf chlorophyll content. Canopies with greater variation in LAD, thus lower ν and μ, have larger values of NDVI, CCI, $SIF_{obs,FR}$, $\frac{SIF_{obs,FR}}{NIR_VR}$, and leaf chlorophyll content, while LAVD is not correlated with these remote sensing metrics. We found positive correlations between leaf chlorophyll content and canopy NDVI, $SIF_{obs,FR}$, and $\frac{SIF_{obs,FR}}{NIR_VR}$, as well. Together, our results show that across our study site during the peak growing season, spatial variability in remote sensing variables is driven by the coordination between LAD and leaf chlorophyll content. These findings provide important context for how we interpret landscape level variability in SIF and $\frac{SIF_{obs,FR}}{NIR_VR}$, and how spatial variation in both can be used to infer differences in plant metabolism.

1. Introduction

The spectral reflectance of vegetative canopies is determined by plant functional and structural properties (Ollinger, 2011). Plant function, which includes eco-physiological processes such as photosynthesis, is linked to foliar biochemical traits (e.g., pigments, proteins). In turn, the optical properties of foliar biochemistry shape spectral reflectance (Gates et al., 1965). Plant canopy structure – the three-dimensional (3D) orientation, density, and vertical distribution of stems and leaves – also affects spectral reflectance across the entire solar domain, particularly enhancing scattering across the near-infrared (NIR) wavelengths (Sellers, 1987; Sellers, 1985), and also affecting the relative contributions of sunlit and shaded vegetation and soil background (Asner, 1998; Myneni and Ross, 1991). Plants have converged on a range of evolutionarily viable combinations of function and structure (Grime, 1977; Mooney and Gulmon, 1979), which create detectable differences in

☆ This article is part of a Special issue entitled: 'Remote Sensing of SIF' published in Remote Sensing of Environment.

* Corresponding authors.
E-mail address: xiyang@virginia.edu (X. Yang).

https://doi.org/10.1016/j.rse.2025.114996
Received 26 December 2023; Received in revised form 6 August 2025; Accepted 22 August 2025
Available online 27 August 2025

canopy reflectance among individuals and species. The effects on reflectance can be direct, such as varying levels of chlorophyll *a*mong species, or they can be indirect. For example, differences in nitrogen content and photosynthetic capacity will affect NIR albedo, primarily as a result of the influence of foliar nitrogen on canopy structure (Knyazikhin et al., 2013; Townsend et al., 2013). Recent advances in remote sensing have provided new ways to measure canopy function and structure. Methods to retrieve solar-induced chlorophyll fluorescence (SIF) have provided a tool to directly measure photosynthetic physiology (Frankenberg et al., 2011; Li et al., 2018; Sun et al., 2017; Yang et al., 2015). Similarly, developments in terrestrial laser scanning (TLS) have allowed canopy structure to be measured in ways previously not possible (Calders et al., 2020; Disney, 2019; Stovall et al., 2021). These tools allow us to connect spectral reflectance to canopy function and structure in a manner that can inform ecological theory.

SIF is an emission of red and far-red photons (640 nm – 850 nm) originating from the excitation of chlorophyll *a* from absorbed sunlight. In principle, remote sensing observations of SIF (SIF_{obs}) at the canopy scale can be defined when only first-order scattering is considered as:

$$SIF_{obs,(\lambda,\Omega)} = PAR \times \left(i_{0,green} \times (1 - \omega_{PAR})\right) \times \phi_{F,\lambda} \times f^{esc}_{(\lambda,\Omega)} \quad (1)$$

where PAR is photosynthetically active radiation, $i_{0,green}$ is the canopy directional interceptance of green components with chlorophyll (Zeng et al., 2022), ω_{PAR} is the single scattering albedo for PAR (transmittance + reflectance). The $i_{0,green} \times (1 - \omega_{PAR})$ term comprises $FPAR_{chl}$, the fraction of PAR absorbed by chlorophyll *a*nd $PAR \times FPAR_{chl} = APAR$. $\phi_{F,\lambda}$ is the quantum yield of steady-state fluorescence at a given wavelength (λ), and $f^{esc}_{(\lambda,\Omega)}$ is the photon escape probability at the viewing angle of the sensor (Ω). $f^{esc}_{(\lambda,\Omega)}$ acts as a scaling factor, ranging from 0 to 1, on the total SIF emission. From Eq. 1, canopy observations of SIF are affected by 1) steady-state biochemistry in the form of canopy chlorophyll content; 2) photosynthetic physiology in the form of $\phi_{F,\lambda}$; 3) canopy structure, which is represented as i_0 and $f^{esc}_{(\lambda,\Omega)}$ in Eq. 1. From Eq. 1, it becomes evident that to isolate $\phi_{F,\lambda}$ from $SIF_{obs,FR}$, the effects of canopy structure (i_0 and $f^{esc}_{(\lambda,\Omega)}$) must accounted for. These effects include the leaf area index (LAI), leaf angle distribution (LAD), and foliar clumping.

Early studies showed empirical relationships between SIF and gross primary productivity (GPP) across scales, from local (Yang et al., 2015) to regional and global (Frankenberg et al., 2011; Li et al., 2018; Sun et al., 2017). Additional studies showed that the relationship between SIF and GPP is more attributable to the APAR and structural terms in Eq.1 than ϕ_F (Dechant et al., 2020; Wieneke et al., 2018; Yang et al., 2018a). In order to use SIF as a photosynthetic proxy, ϕ_F must be connected to the quantum yield of photochemistry (ϕ_P), which controls the electron supply for the light-independent reactions of photosynthesis (Frankenberg and Berry, 2018; Magney et al., 2020; van der Tol et al., 2014). This is not a straightforward endeavor, as ϕ_F competes with ϕ_P and non-photochemical quenching (NPQ) for excitation energy from APAR. The competition among these processes is complex and dynamic, operating at timescales of milliseconds to minutes (Sun et al., 2023a). Moreover, the relationship between ϕ_F and ϕ_P exhibits non-linearity that is affected by light intensity and environmental stress (Gu et al., 2019; Magney et al., 2020; Porcar-Castell et al., 2014; Sun et al., 2023b; van der Tol et al., 2014). Under light-saturating conditions ϕ_F and ϕ_P are linearly related, but this linearity can be disrupted due to sudden adjustments in photosynthesis (Helm et al., 2020; Marrs et al., 2020; Wu et al., 2022). Interestingly, the same sensitivity to changes in photosynthetic physiology that decouples ϕ_F and ϕ_P enables SIF measurements to be used to detect stress responses of vegetation (Damm et al., 2022; Martini et al., 2022; Sun et al., 2023b; Wang et al., 2022). SIF and ϕ_F also covary with foliar biochemical properties related to photosynthesis (Sun et al., 2023b, Sun et al., 2023a; Zhang et al., 2014). Nitrogen treatment experiments have shown differences in SIF in crops and natural systems (Ač et al., 2015; Jia et al., 2021; Migliavacca et al., 2017). SIF and $\phi_{F,\lambda}$ are correlated with chlorophyll content at the leaf scale (Tubuxin et al., 2015), while canopy scale observations covary with pigment pools (Kim et al., 2021; Pierrat et al., 2022) using the chlorophyll:carotenoid index (CCI, Gamon et al., 2016), an optical proxy for chlorophyll (Wong et al., 2020).

Optical proxies of canopy structure have also been important for SIF and inferring photosynthetic productivity. NIR wavelengths have long been known to be sensitive to canopy structure, dating back to formative studies on NDVI and its precursors (Colwell, 1974; Jordan, 1969; Tucker, 1979). It was recognized that NDVI could be used to estimate FPAR, a key parameter in light-use efficiency models of GPP (Running et al., 2004). In principle NIR_V is a better proxy for FPAR than NDVI (Sellers, 1987), but non-vegetative components are often an appreciable fraction of total scene NIR reflectance (NIR_T), particularly at the coarse resolutions of satellite imagery. Recently, Badgley et al. (2017) showed that NIR_V can be approximated as the product of NDVI and NIR_T, with NDVI representing the proportion of NIR reflectance attributable to vegetation. This approach for approximating NIR_V has been found to be a stronger predictor of GPP than NDVI or SIF across vegetation types and across spatial scales (Badgley et al., 2019; Baldocchi et al., 2020; Dechant et al., 2022, Dechant et al., 2020). Importantly, NIR_V shares a physical basis with far-red SIF which allows $f^{esc}_{(\lambda,\Omega)}$ to be approximated (Zeng et al., 2019). Additional modeling and field-based analyses showed that ϕ_F can be derived using the radiance equivalent of NIR_V (NIR_VR, Zeng et al., 2022).

When considering the spatial patterns of canopy reflectance and SIF, it is important to recognize that plants are biological organisms that have been shaped by evolutionary and ecological principles (Field, 1991; Gamon et al., 2019; Ollinger, 2011). Plants coordinate canopy function and structure to maximize whole-plant carbon gain given the biotic and abiotic environments in which they are growing (Givnish, 2020; Hirose, 2005; Horn, 1971; Monsi and Saeki, 1953). Foliar resources such as nitrogen and other elements are distributed based on the spatial arrangement of leaves through the canopy (Ellsworth and Reich, 1993; Niinemets, 2010; Yang et al., 2023). This distribution leads to a coordination between function and structure that modulates photosynthetic capacity and leaf chlorophyll content (Croft et al., 2017; Kattge et al., 2009). The result of this coordination has important implications for vegetation reflectance, derived spectral indices, and SIF. For example, NDVI is affected by NIR scattering from canopy structure and by leaf chlorophyll content (Gamon et al., 1995; Gitelson and Merzlyak, 1997). Since the arrangement of canopy structure also affects leaf chlorophyll content, NDVI and other vegetation indices can be viewed as indicators of different functional-structural configurations that evolution has selected for across individuals and species. These biophysical linkages also extend to SIF. Canopy structure directly affects $i_{0,green}$ and $f^{esc}_{(\lambda,\Omega)}$ in Eq. 1. The coordination between function and structure indirectly affects $(1 - \omega_{PAR})$ and ϕ_F via the influence chlorophyll *a*nd foliar nitrogen (Koffi et al., 2015; Migliavacca et al., 2017; Verrelst et al., 2016).

Given the connections between canopy function and structure, one might expect that remotely sensed observations of pigments and photosynthetic physiology covary with canopy structure. Studies investigating these covariations have been lacking, largely due to the difficulty in measuring canopy structure. TLS instrument quality and data processing has improved dramatically in the last decade (Calders et al., 2020; Disney, 2019), allowing accurate and rapid estimates of LAD and LAI (Jupp et al., 2009; Stovall et al., 2021; Vicari et al., 2019). In particular, leaf angle and LAD is an understudied component of canopy structure that is essential for plant ecophysiology (Close and Beadle, 2006; Hirtreiter and Potts, 2012) and is known to affect remote sensing observations (McNeil et al., 2023; Yang et al., 2023). However, no empirical studies have examined the relationship between LAD and remote sensing data. Additionally, there are few studies examining the spatial patterns in SIF and reflectance at the canopy or landscape scale

(Maguire et al., 2021; Zeng et al., 2022). These questions require high spatial resolution data that can only be obtained from a fixed-wing aircraft or uncrewed aerial system (UAS). Most canopy-scale studies of SIF rely on tower-based observation systems, which have a high temporal resolution but only measure either one canopy, or multiple canopies, typically with inconsistencies in viewing zenith angle (Dechant et al., 2020; Kimm et al., 2021; Pierrat et al., 2022, Pierrat et al., 2021). In this study, we combine a novel UAS-based system with concurrent TLS data and foliar sampling to answer the question, "Does canopy structure covary with reflectance indices, SIF, and $\phi_{F,\lambda}$, across individual tree canopies?" We hypothesize that LAD and LAI will be correlated with remotely sensed variables of NIR_V, reflectance indices, SIF, and $\phi_{F,\lambda}$. We examine these relationships across two datasets collected under contrasting phenological stages; one dataset collected during the peak growing season, and another collected during autumn leaf senescence when nutrients are being remobilized and reallocated to other tissues in preparation for winter dormancy.

2. Materials and methods

2.1. Overview

Our study site was Milton Airfield (37.9941°N, −78.3976°W, Fig. 1) – an abandoned airfield now used by radio-controlled aircraft hobbyists with adjacent regenerated stands of deciduous broadleaf (DBF) and evergreen needleleaf (ENF) trees. We developed a novel UAS called FluoSpecAir (Fig. 2, Section 2.2) to measure spatiotemporal patterns in SIF and VNIR reflectance (400 nm – 850 nm) across individual tree canopies at Milton Airfield on clear-sky days. For this study, we collected two datasets – one collected at the onset of foliar senescence in 2020, and another during the peak growing season of 2021. We refer to these datasets as "foliar senescence" and "peak growing season" respectively. For each dataset, we supplemented FluoSpecAir flights with 3D structural data from a subset of canopies using terrestrial laser scanning (Section 2.3) and foliar sampling (Section 2.4).

The foliar senescence dataset was collected on three separate weeks, spaced approximately 14 days apart. Measurements began on DOY 251, 267, and 282, respectively. FluoSpecAir was flown at four separate time intervals: 7:00–8:00, 11:00–12:00, 12:00–13:00, and 15:00–16:00 EST. Each flight flew predetermined waypoints that covered individual canopies of American sycamore, black cherry, red maple, and tulip poplar from the DBF stand, and canopies of eastern white pine from the ENF stand (Fig. 1, Table 1). Flights were repeated across 2–3 days to ensure sufficient spatiotemporal coverage and good data quality. Following the completion of flights, a subset of canopies targeted by FluoSpecAir were scanned using TLS. We collected foliar samples for the flights pertaining to DOY 267 and 282.

The peak growing season dataset was collected on four separate weeks (DOY 133, 148, 188, and 217). FluoSpecAir flights were made hourly from 7:00–16:00 EST, with another repeat day of flights. The peak growing season dataset was collected from a different but nearby set of waypoints with some canopy overlap, including black cherry, eastern white pine, red maple, and tulip poplar (Table 1). FluoSpecAir suffered a malfunction on the week pertaining to DOY 148, and thus, we were only able to make two flights at 7:00 and 8:00. For each week of FluoSpecAir flights, we scanned a subset of canopies using TLS. Foliar traits were sampled on days following DOY 148 and 188.

2.2. FluoSpecAir

The UAS used in FluoSpecAir is a DJI Matrice 600 Pro (M600 Pro) with a D-RTK real-time kinematics mobile GNSS station, and a Zenmuse X2 camera. Autonomous flight and data acquisition were controlled using an onboard Raspberry Pi 3 Model B connected to the A3 flight controller on the M600 Pro. Using the DJI Onboard SDK (version 3.9), we developed an autonomous flight script that 1) centered on coordinates for each canopy, with the UAS positioned 15 m above the canopy and the aircraft "nose" always oriented north; 2) made measurements of downwelling irradiance and upwelling radiance at nadir; 3) initiated video capture from the Zenmuse X2 camera for the entirety of the upwelling radiance measurement. Coordinates for each canopy were selected by manually flying the M600 Pro over individual canopies. Using the Zenmuse X2 video feed, we recorded the coordinates from the RTK antenna onboard the M600 Pro when the fiber field of

Fig. 1. Aerial view of the field site at Milton Airfield. Individual canopies measured in this study are shown, with the white lettering corresponding to the ID listed in Table 1. Light blue circles indicate deciduous broadleaf forest (DBF) canopies and light yellow triangles represent evergreen needleleaf forest (ENF) canopies. The takeoff and landing location of FluoSpecAir is outlined in black. (For interpretation of the references to colour in this figure legend, the reader is referred to the web version of this article.)

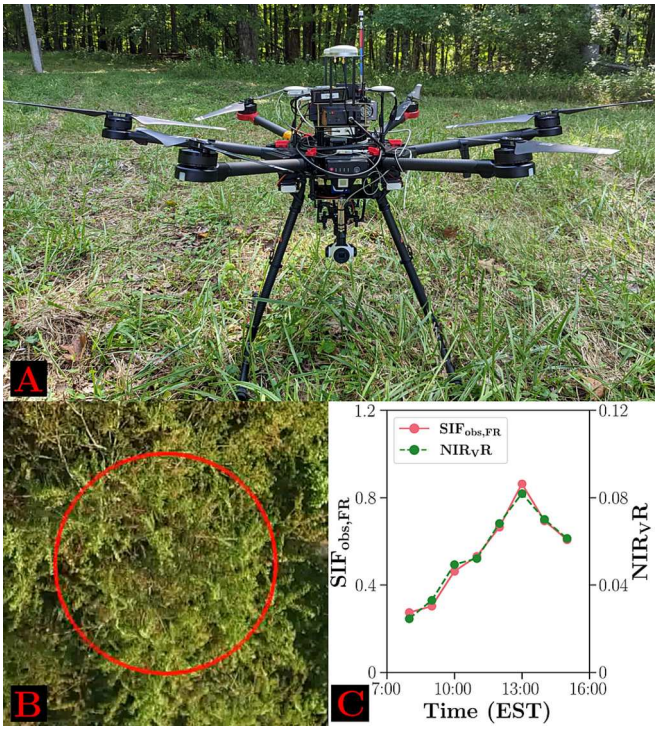

Fig. 2. Panel A) Picture of the FluoSpecAir observation platform used in this study. FluoSpecAir uses a M600 Pro hexacopter with a modified FluoSpec2 payload to measure SIF and VNIR reflectance of individual plant canopies. Panel B) Still frame taken from a video during upwelling radiance collection. The red circle overlays the fiber optic FOV with respect to the Zenmuse X2 camera. We ensured that FluoSpecAir was positioned over all targeted canopies by checking each recorded video feed (see Fig. S1 for examples). Panel C) Daily pattern of $SIF_{obs,FR}$ (mW m^{-2} sr^{-1} nm^{-1}) and NIR_VR (W m^{-2} sr^{-1} nm^{-1}) for the canopy shown on the day of flight. (For interpretation of the references to colour in this figure legend, the reader is referred to the web version of this article.)

view (FOV) was covering the targeted canopy (see the following paragraphs for details). Using RTK positioning for FluoSpecAir measurements is critical – we compared the accuracies of the RTK antennas and standard A3 antennas on the M600 Pro against 10 surveyed points and noted X/Y/Z accuracies of ≤5 cm using RTK, while A3 accuracy was ≥1 m (data not shown). For time and safety considerations, the take-off and landing of the M600 Pro were performed manually by the M600 Pro pilot.

FluoSpecAir uses a modified FluoSpec2 (Yang et al., 2018b) dual-spectrometer system consisting of an Ocean Insight (Dunedin, Florida, United States) QEPro spectrometer, which measures wavelengths between 730 nm – 785 nm (100 μm slit, 0.31 nm full-width half maximum (FWHM)), and an Ocean Insight Flame spectrometer, which measures between 340 nm – 1040 nm (25 μm slit, 3.28 nm FWHM at 546 nm). Fiber optics for measuring downwelling irradiance and upwelling radiance were connected to a rotating prism, which selectively directs incoming light from either fiber to a BF19Y2LS02 bifurcated fiber (Thorlabs Inc., Newton, NJ, USA) connected to the two spectrometers. The downwelling irradiance fiber used an Ocean Insight CC-3 cosine corrector and was calibrated for irradiance using an Ocean Insight HL-3 light source. The upwelling radiance fiber used a Gershun tube kit (Ocean Insight) to restrict the field of view to 6°, and was calibrated for radiance using a Labsphere 8 in. HELIOS integrating sphere (15.24 cm) (Labsphere, North Sutton, New Hampshire, United States). The QEPro had a thermoelectric cooler which kept the detector temperature stable around −10 °C. For correcting the dark signal on the QEPro we used the method by Yang et al. (2018a, 2018b), which creates a lookup table of

Table 1
The list of canopies measured with FluoSpecAir in this study. The ID field is a unique field-assigned identifier for a given individual. DOY coverage signifies when FluoSpecAir data is available for a canopy. ^{T} Signifies TLS scan of canopy on DOY.

ID	Species	Common name	PFT	DOY coverage
1	*Acer rubrum*	Red maple	DBF	251, 267, 282
3	*Platanus occidentalis*	American sycamore	DBF	251, 267, 282
4	*Acer rubrum*	Red maple	DBF	133^T, 148, 217^T, 251, 267, 282
7	*Acer rubrum*	Red maple	DBF	267^T, 282^T
8	*Liriodendron tulipifera*	Tulip poplar	DBF	133^T, 148, 188^T, 217^T, 267^T, 282^T
10	*Liriodendron tulipifera*	Tulip poplar	DBF	133^T, 148, 188^T, 217^T, 267^T, 282^T
11	*Prunus serotina*	Black cherry	DBF	133^T, 188^T, 217^T, 251, 267^T, 282^T
12	*Prunus serotina*	Black cherry	DBF	133, 148, 188, 251, 267
13	*Prunus serotina*	Black cherry	DBF	267, 282
14	*Acer rubrum*	Red maple	DBF	133^T, 148, 188^T, 217^T, 251, 267^T, 282^T
15	*Liriodendron tulipifera*	Tulip poplar	DBF	251, 267^T, 282^T
16	*Pinus strobus*	Eastern white pine	ENF	133, 148, 188^T, 217^T, 251, 282^T
17	*Pinus strobus*	Eastern white pine	ENF	251, 267^T, 282^T
18	*Pinus strobus*	Eastern white pine	ENF	251, 267^T, 282^T
19	*Pinus strobus*	Eastern white pine	ENF	251
20	*Pinus virginiana*	Virginia pine	ENF	133, 188^T, 217^T
21	*Liriodendron tulipifera*	Tulip poplar	DBF	133^T, 148, 188^T, 217^T
22	*Acer rubrum*	Red maple	DBF	133^T, 148, 188^T, 217^T
26	*Pinus strobus*	Eastern white pine	ENF	188^T, 217^T
30	*Pinus resinosa*	Red pine	ENF	217

dark current spectra across temperature values and integration times, and assumes dark current is linearly correlated with integration time at a given temperature. The Flame instrument lacked a TEC cooler and thus could not be temperature stabilized. To account for the dark current, we made measurements of dark spectra using the Flame before and after each flight, and averaged both values for the dark spectra. We assumed that the temperature of the Flame spectrometer stayed constant before, during, and after each flight. Inspection of pre-flight and post-flight dark spectra showed no noticeable differences between the two, providing some basis for this assumption.

The downwelling radiance fiber was mounted on a bracket in order to maintain a fixed position relative to the Zenmuse X2 camera and gimbal – this enabled alignment of the fiber FOV with the video output from the camera. Projecting the fiber FOV onto the video output was achieved by shining a light through the fiber in a dark room while recording video feed from the camera. As a result, for every recorded video of upwelling radiance data collection, we were able to accurately identify if measurements were made from the targeted canopies for this study. With each measurement taken at a distance of 15 m above each canopy, the spot size was approximately 2 m^2 for all canopies.

We used the QEPro data to retrieve far-red SIF ($SIF_{obs,FR}$) in mW m^{-2} sr^{-1} nm^{-1} in the O_2-A band using the spectral fitting method (Meroni et al., 2010). We used a fitting window of 759.5 nm – 761.5 nm (Chang et al., 2020) with linear functions. In our retrieval of SIF, we did not account for any atmospheric attenuation of the SIF signal based on the distance from each target to the sensor. We measured this effect to be minimal based on an experimental flight where we examined how $SIF_{obs,FR}$ changed as a function of height against a non-fluorescence target of asphalt pavement (Fig. S2). We used reflectance from the Flame to calculate NDVI and CCI using the equations:

$$NDVI = \frac{r858 - r648}{r858 + r648} \quad (2)$$

$$CCI = \frac{r530 - r670}{r530 + r670} \quad (3)$$

Where r represents reflectance at a wavelength in nm. Additionally, we calculated NIR_V and NIR_VR as:

$$NIR_V = NDVI \times r780 \quad (4)$$

$$NIR_VR = NDVI \times L_{780} \quad (5)$$

Where L_{780} is radiance at 780 nm. For radiance and reflectance at 780 nm, we used data from the QEPro.

Data were quality controlled and filtered out based on 1) whether upwelling radiance measurements occurred over the targeted canopy and were free of shadows based on the video feed (see Fig. S1 for examples); 2) whether there were clear and stable sky conditions based on the video feed and irradiance values; 3) spectral shape (was there a peak in green reflectance, red edge, and NIR plateau, indicating a vegetative spectral signature) and magnitude of NIR reflectance ($0.2 \leq$ NIR reflectance ≤ 0.6); 4) $SIF_{obs,FR}$ values <0 mW m^{-2} sr^{-1} nm^{-1}. We made no corrections for any potential roll and pitch effects on upwelling or downwelling measurements. These effects were observed to be minimal based on observing the video feed from each measurement.

We estimated $\phi_{F,FR}$ using the conceptual approach by Zeng et al. (2022), who showed that $\frac{SIF_{obs,FR}}{NIR_VR}$ is proportional to $\phi_{F,FR}$. NIR_VR and $SIF_{obs,FR}$ are known to be strongly correlated with each other – the reason for this being they share a physical basis that can be seen when comparing Eq. 1 to the following equation:

$$NIR_VR = S_{NIR} \times \left(i_{0,green} \times \omega_{NIR}\right) \times f^{esc}_{(\lambda,\Omega)} \quad (6)$$

NIR_VR and $SIF_{obs,FR}$ are dependent on incoming solar radiation (PAR for SIF, incoming solar radiation in the NIR (S_{NIR}) for NIR_V), canopy interceptance, and $f^{esc}_{(\lambda,\Omega)}$. One key difference is that NIR_VR is affected by the single scattering albedo for NIR wavelengths (ω_{NIR}), whereas for SIF, $(1 - \omega_{PAR})$ is the absorbance in the visible domain. Although $f^{esc}_{(\lambda,\Omega)}$ depends upon wavelength, NIR photons absorb and scatter similarly to far-red photons from SIF, particularly at wavelengths $\geq$750 nm. Thus, $f^{esc}_{(\lambda,\Omega)}$ should functionally be similar for both. This approach is contingent on NIR_VR and $SIF_{obs,FR}$ being measured from the same field of view, otherwise mismatches in Ω and/or the ratio of diffuse radiation will introduce uncertainty into the estimation of $\phi_{F,FR}$. Additionally, an implicit assumption is that the ratio between $(1 - \omega_{PAR})$ and ω_N is constant within and across taxa, and throughout time. We explain how all variables in Eqs. 1 and 6 are calculated in Section 2.5.

2.3. Terrestrial laser scanner

In this study, we made 3D scans using a Faro Focus 120 (Faro Technologies, Lake Mary, FL, USA) for all measurement weeks, with the exception of one week (week 31) in the peak growing season where we used a Leica RTC 360 (Leica Geosystems, St. Gallen, CH) TLS. The difference in data collected by each instrument has not been reported in the literature, nor was it possible to do so for this study. We note that the Leica TLS collected approximately five times as many points per second than the Faro TLS, creating denser and more detailed point clouds. FluoSpecAir canopies were scanned from multiple positions to create a 360° reconstruction. In some instances, a 360° reconstruction was not possible due to occlusion from surrounding canopies. Scans were made along a track that was designed to maximize coverage of FluoSpecAir canopies from each scan position. We staked a grid of 14.7 cm diameter reference balls to co-register individual TLS scans to one another. On average, each individual scan shared six reference balls with any other scan, and no scans shared fewer than four reference balls. Registration of TLS scans was performed using the instrument's respective software package – for the Focus 3D we used Faro SCENE and for the Leica RTC 360, we used Register 360. Reported alignment error averaged around 5 mm for registered scans. Individual trees from registered point clouds were then manually extracted.

We applied the TLSLeAF algorithm (Stovall et al., 2021) to create 10 cm^3 voxels of leaf inclination angles (θ_L) from the tree point clouds. Using the mean θ_L for each voxel, we quantified LAD using; 1) a beta distribution (Goel and Strebel, 1984) parameterized by ν and μ; 2) the leaf inclination distribution function LIDF (Verhoef, 1997) which is parameterized by LIDFa and LIDFb – these are parameters used in radiative transfer models (RTMs) of canopies such as SCOPE (van der Tol et al., 2009); 3) the mean and standard deviation of θ_L of all voxels. We used a voxel-based method (Hosoi and Omasa, 2006) to calculate vertical profiles of leaf area voxel density (LAVD). The contact frequency for each vertical slice was calculated using points classified as vegetation from the TLSLeAF output. We then multiplied the contact frequency by a correction factor of 1.1 that accounts for leaf inclination angle to calculate the leaf area voxel density (Li et al., 2017). We used the same voxel resolution for LAD and LAVD calculations (10 cm^3 as recommended by TLSLeAF). We computed the LAI by summing LAVD across all vertical bins.

We calculated LAD parameters as a function of the cumulative vertical LAVD to account for differences in vertical foliage density (Fig. 3). Representing the top of the canopy as 0 %, we calculated the canopy height where a specified cumulative LAVD is found. Next, we selected all angle voxels greater than or equal to the calculated height, and calculated the corresponding beta distribution and LIDF parameters, and the mean and standard deviation of angle voxels. Optimal LIDF parameters were calculated by applying a numerical minimization to an algorithm provided by Verhoef (1997), which generates the cumulative leaf inclination distribution for any combination of LIDFa and LIDFb. We used the lmfit package in Python 3.8 to apply a least-squares minimization using the trust region reflective method. LIDFa and LIDFb were constrained such that $|LIDFa| + |LIDFb| \leq 1$ (Verhoef, 1997). The optimization was performed on the probability density of observed leaf angles using one-degree bins. We calculated the probability density from the algorithm provided by Verhoef (1997) by taking the difference in cumulative distribution between inclination intervals θ_1 and θ_2, where the interval was one degree.

2.4. Field and foliar sampling

We collected a limited set of foliar samples for the foliar senescence and peak growing season datasets. Foliar samples were collected on flights corresponding to DOY 148, 188, 267, and 282. Sun-exposed, top of canopy, foliar samples were collected from canopies using a modular pole pruner. We selected 1–5 non-chlorotic leaves per canopy. Foliar sampling occurred in the morning and midday; upon obtaining samples, they were immediately placed into plastic bags and stored in a dark cooler with ice. In the afternoon, samples were returned to the laboratory where they were measured for the projected area using a LI-3000C (LiCor Biosciences, Lincoln, NE, USA) leaf area meter. Foliar samples were then measured for spectral reflectance – for the foliar senescence dataset we used an ASD FieldSpec 3 (ASD Inc., Boulder, CO, USA) and the peak growing season dataset used an SVC HR-1024i (Spectra Vista Corp, Poughkeepsie, NY, USA). The leaf reflectance was measured by each instrument using a plant contact probe with an external light source. For ENF species, fresh spectra were measured by arranging needles together in a singular mat with no open spaces between needles. We measured reflectance spectra at five positions for each leaf, and averaged all scans. Following projected area and reflectance measurements, foliar samples were oven-dried at 60 °C for 48 h to measure the dry mass and calculate LMA.

Spectral reflectance from 400 nm – 950 nm was inverted using PROSPECT-D (Féret et al., 2017) to retrieve estimates of chlorophyll a +

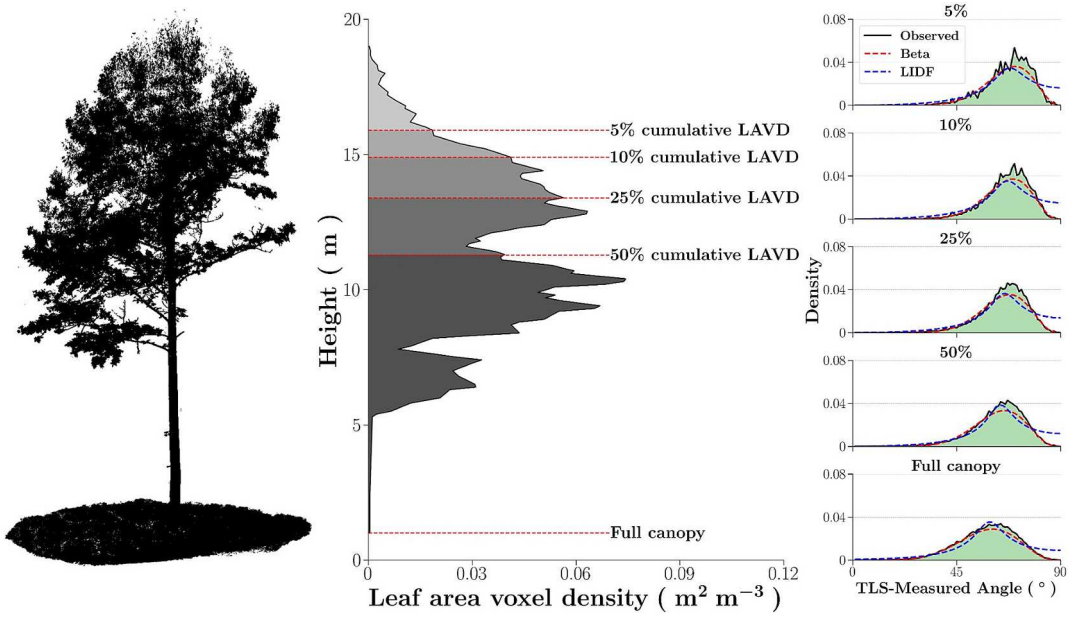

Fig. 3. A visualization of how LAD parameters were calculated using our point cloud data. In this example, we used ID 10 from DOY 217 (Table 1). For an isolated tree (left panel), we calculated the vertical LAVD profile using all co-registered point cloud data. In this example, we show the height of the tree at which corresponds to 5 %, 10 %, 25 %, 50 %, and 100 %, of the cumulative LAVD ($m^2\ m^{-3}$). The probability density function using the beta and LIDF distributions, and the observed distribution, for each cumulative LAVD is shown on the right panels.

b (leaf chlorophyll content) and leaf carotenoid content. PROSPECT-D was inverted using a numerical minimization, with a least-squares curve fit with a trust region reflective algorithm using the lmfit package. We estimated the mesophyll thickness, the chlorophyll a + b content, the carotenoid content, the anthocyanin content, brown pigments, and water thickness, parameters. We used the leaf LMA as the dry mass parameter. We calculated leaf ω_{PAR} averaging reflectance + transmittance from 400 nm – 700 nm. Leaf ω_{NIR} was calculated by averaging reflectance + transmittance from 777 nm – 783 nm.

2.5. Analysis

We examined the spatial distributions of canopy NDVI, canopy NIR_V, canopy CCI, $SIF_{obs,FR,}$ and $\frac{SIF_{obs,FR}}{NIR_VR}$, ν, and μ, across all individuals, and how they varied diurnally, across the foliar senescence and peak growing season datasets. We used the Tukey-Kramer approach to compare how distributions of each variable changed for DBF species within and across each dataset. We did not make statistical comparisons of ENF distributions because of limited observations. We then analyzed the relationships of $SIF_{obs,FR}$ and $\frac{SIF_{obs,FR}}{NIR_VR}$ with canopy NDVI, canopy NIR_V, and canopy CCI. For each dataset, we show the relationships among variables for each week of FluoSpecAir measurements. We used all data from all flights and averaged observations from multiple days on an hourly basis. Additionally, we examined if the relationships among variables vary diurnally by averaging observations for certain times of the day. Specifically, we examined relationships during the morning (7:00–9:00), midday (11:00–13:00), and afternoon (14:00–16:00).

We used linear mixed effects models to understand the spatiotemporal relationship of cumulative LAVD and LAD with our remote sensing observations. We chose this method because a simple linear regression analysis would violate the assumption of independence. The foliar senescence and peak growing season datasets consist of repeat canopy observations across different weeks, thus our analysis needed to account for effect of each canopy at different points in time. We used the model structure:

$$y = X\beta + Z\mu + \varepsilon \quad (7)$$

Where y is the outcome variable (canopy NDVI, canopy CCI, $SIF_{obs,FR}$, or $\frac{SIF_{obs,FR}}{NIR_VR}$), X is the predictor variable vector (cumulative LAVD, ν, μ, LIDFa, and LIDFb), β is the fixed-effects regression coefficients, Z is the design matrix for the random effect (tree ID), μ is the vector for the random effects (the random complement to the fixed β), and ε is the model residuals not explained by the model Xβ + Zμ. We constructed models for the foliar senescence and peak growing season datasets, using canopies that had concurrent FluoSpecAir and TLS observations (Table 1). The outcome variables were calculated as the mean daily value using all hourly data for each canopy and week. Linear mixed effects models were generated in R using the lme4 package. We report the marginal R^2 (R^2_m), which is the proportion of total variance explained by the fixed effect, and the conditional R^2 (R^2_c), which is the proportion of variance explained by both fixed and random effects (Nakagawa et al., 2017). Model evaluation and calculation of R^2_m and R^2_C was done using the mlmtools package in R.

We present the model relationships using 10 % of the cumulative LAVD ($LAVD_{10\%}$). We report these variables with the percentage subscripted, such that $\nu_{10\%}$ and $\mu_{10\%}$ would represent ν and μ at 10 % of the cumulative LAVD. This percentage was chosen based on an analysis to determine what portion of the canopy is most relevant to our remote sensing data. Using the same model structure described in the previous paragraph, we built models using 1 % increments of the cumulative LAVD, starting from 1 % and ending at 100 %. The highest R^2_c values for models using μ were found approximately between 10%–20 % of the cumulative LAVD, while R^2_c values for ν typically reached their maximum between 50 % – 70 % (Fig. S3).

We performed an exploratory analysis to provide greater contextual meaning to beta distribution parameters ν and μ. Using the underlying equations for ν and μ (Eq. A1 – A3), we showed how the mean and variance affect the shape of the beta distribution. We developed a more intuitive equation for explaining μ. To test the generality of our findings, we compared our results to 100 randomly generated beta distributions, constraining the range of ν and μ in our simulated data to the range of our observational data.

As a check on the assumption that $\frac{SIF_{obs,FR}}{NIR_VR}$ is proportional to $\phi_{F,FR}$, we rearranged Eq. 1 and Eq. 6 to the following:

$$\frac{SIF_{obs,FR}}{NIR_VR} = \frac{PAR}{S_{NIR}} \times \frac{1-\omega_{PAR}}{\omega_{NIR}} \times \phi_{F,FR} \quad (8)$$

We used our field observations to examine the potential influence of the first two terms in eq. 3 on $\frac{SIF_{obs,FR}}{NIR_VR}$. S_{nir} was calculated as incoming irradiance at 780 nm from the QEPro, while foliar samples were used to calculate $\frac{1-\omega_{PAR}}{\omega_{NIR}}$. ω_{PAR} was calculated by averaging reflectance + transmittance from 400 nm – 700 nm. ω_{NIR} was calculated by averaging across wavelengths 777 nm – 783 nm. $\frac{PAR}{S_{NIR}}$ was approximated by averaging all daily values of PAR/S_{nir} for individual plant canopies with concurrent foliar measurements of ω_{PAR} and ω_{NIR} during a sampling week.

Finally, we analyzed relationships between leaf chlorophyll content and remote sensing variables and canopy structural parameters. Due to limited foliar sampling during the peak growing season dataset, we show relationships from data collected on DOY 188. For the foliar senescence dataset, we show relationships from data collected on DOY 267. When examining relationships between leaf chlorophyll content and our structural metrics, we used whole-canopy values (e.g. $LAVD_{100\%}$, $\nu_{100\%}$ and $\mu_{100\%}$). Whole-canopy values are more representative of coordination between leaf chlorophyll content and canopy structure, as they reflect the patterns of resource allocation made at the level of the individual.

3. Results

3.1. Spatiotemporal patterns of optical remote sensing data and LAD

Canopy NDVI, canopy CCI, $SIF_{obs,FR}$, and $\frac{SIF_{obs,FR}}{NIR_VR}$, were larger in the peak growing season than during foliar senescence for DBF canopies (Fig. 4). Canopy NIR_V, $LAVD_{10\%}$ and beta distribution parameters $\nu_{10\%}$ and $\mu_{10\%}$ did not differ as much between the two datasets (Fig. 4). We note that for $SIF_{obs,FR}$, and $\frac{SIF_{obs,FR}}{NIR_VR}$, the last week of flights for the peak growing season dataset tended to show no differences against observations from the foliar senescence dataset (Fig. 4d – 4e). $LAVD_{10\%}$ and $\nu_{10\%}$ values were slightly higher during the peak growing season, but not large enough to differ significantly from measurements made during foliar senescence, except for DOY 217 (Fig. 4f, h). We observed no differences in the mean or standard deviation of leaf angle ($mean_{10\%}$, $sd_{10\%}$, Fig. S4f – S4g), though peak growing season distributions had comparatively more canopies with a higher mean leaf angle. TLS observations for this week were made using the Leica RTC 360, which as mentioned, collected 5× as many points compared to the Faro Focus TLS used on all other weeks.

During the peak growing season, canopy NDVI was constant among DBF species, with a mean value of 0.88 for flights on DOY 133,148, and 217. Canopy NDVI was larger on DOY 188, with a mean value of 0.91 (Fig. 4a). Canopy NIR_V peaked on DOY 148 and declined the following weeks, with DOY 217 showing the lowest mean canopy NIR_V. Canopy CCI declined throughout the peak growing season for DBF species, with a lower mean value for DOY 217 compared to DOY 133, though we note that DOY 133 exhibited larger variation (Fig. 4c). Similarly, $SIF_{obs,FR}$ and $\frac{SIF_{obs,FR}}{NIR_VR}$ declined across the peak growing season (Fig. 4c – 4d), although we observed an increase in both for DOY 148. We observed decreases in canopy NDVI among DBF species during foliar senescence (Fig. 4a). Mean canopy NDVI declined by approximately 9 % from DOY 251 (canopy NDVI = 0.87) to DOY 282 (canopy NDVI = 0.79). Canopy NIR_V, canopy CCI, $SIF_{obs,FR}$, and $\frac{SIF_{obs,FR}}{NIR_VR}$ did not change across the sampling period for DBF species (Fig. 4b – 4e), though the distributions changed, particularly when comparing DOY 251 and DOY 282. Given the limited number of ENF canopies for both datasets, we opted not to make any statistical or qualitative comparisons with either dataset.

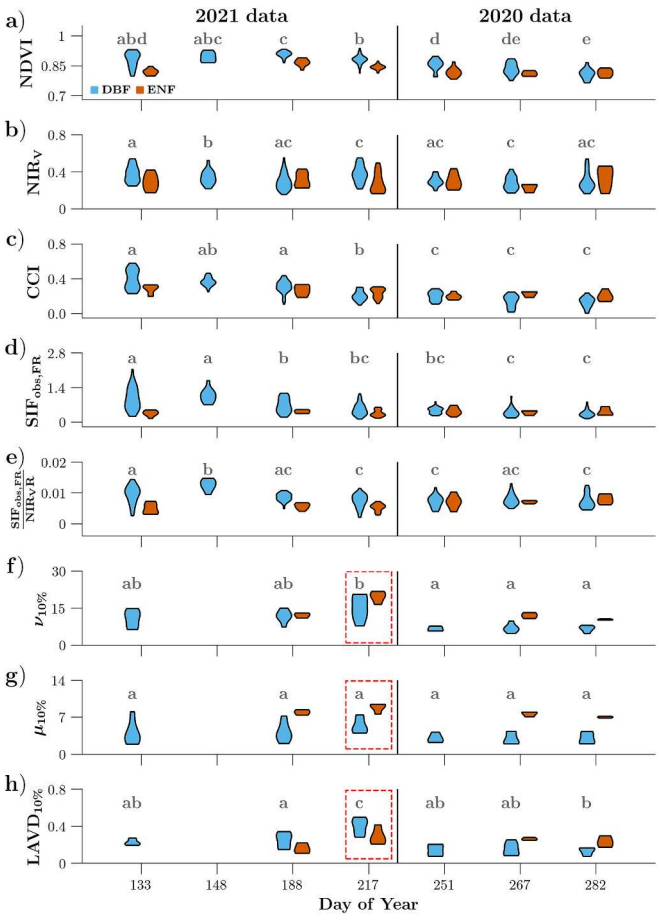

Fig. 4. Violin plots of canopy (a) NDVI, (b), NIR_V, (c) CCI, (d) $SIF_{obs,FR}$ (mW m^{-2} sr^{-1} nm^{-1}), (e) $\frac{SIF_{obs,FR}}{NIR_VR}$, (f) $\nu_{10\%}$, (g) $\mu_{10\%}$, and (h) $LAVD_{10\%}$ (m^2 m^{-3}), for DBF and ENF canopies, using all observations for each week that FluoSpecAir was flown. Significant differences in mean values between observation weeks are indicated by lowercase letters in gray ($P < 0.001$) for DBF canopies. The red outlined box in panels f – h denote TLS measurements made with a Leica RTC 360. Observations from the peak growing season are shown to the left of the vertical line and observations from foliar senescence are shown to the right of the line. (For interpretation of the references to colour in this figure legend, the reader is referred to the web version of this article.)

During the peak growing season, spatial variation in $SIF_{obs,FR}$ was more strongly related to canopy CCI than canopy NDVI (Fig. 5). We observed significant relationships between $SIF_{obs,FR}$ and NIR_V, though they were mostly weaker compared to canopy NDVI or canopy CCI. With respect to $\frac{SIF_{obs,FR}}{NIR_VR}$; canopy NDVI had a stronger relationship with $\frac{SIF_{obs,FR}}{NIR_VR}$ than canopy CCI, while no relationship with canopy NIR_V was observed. These patterns were consistent across the morning, midday, and afternoon (Fig. S5). The R^2 values of spatial relationships at individual times were larger compared to Fig. 5, which pools all data across all times. The R^2 of spatial relationships declined as the peak growing season progressed – this is particularly noticeable when examining relationships of canopy NDVI and canopy CCI with $\frac{SIF_{obs,FR}}{NIR_VR}$. We observed no significant relationships across canopy NDVI, and canopy CCI, with $SIF_{obs,FR}$ or $\frac{SIF_{obs,FR}}{NIR_VR}$ across the foliar senescence dataset (Fig. 6). Canopy NIR_V was significantly correlated with $SIF_{obs,FR}$ on DOY 251. Similarly, we observed minimal correlations between variables when looking at data across individual times of day. Of note, midday observations, which minimize solar angle issues, showed only one significant correlation between canopy NDVI and $\frac{SIF_{obs,FR}}{NIR_VR}$ on DOY 282 (Fig. S6).

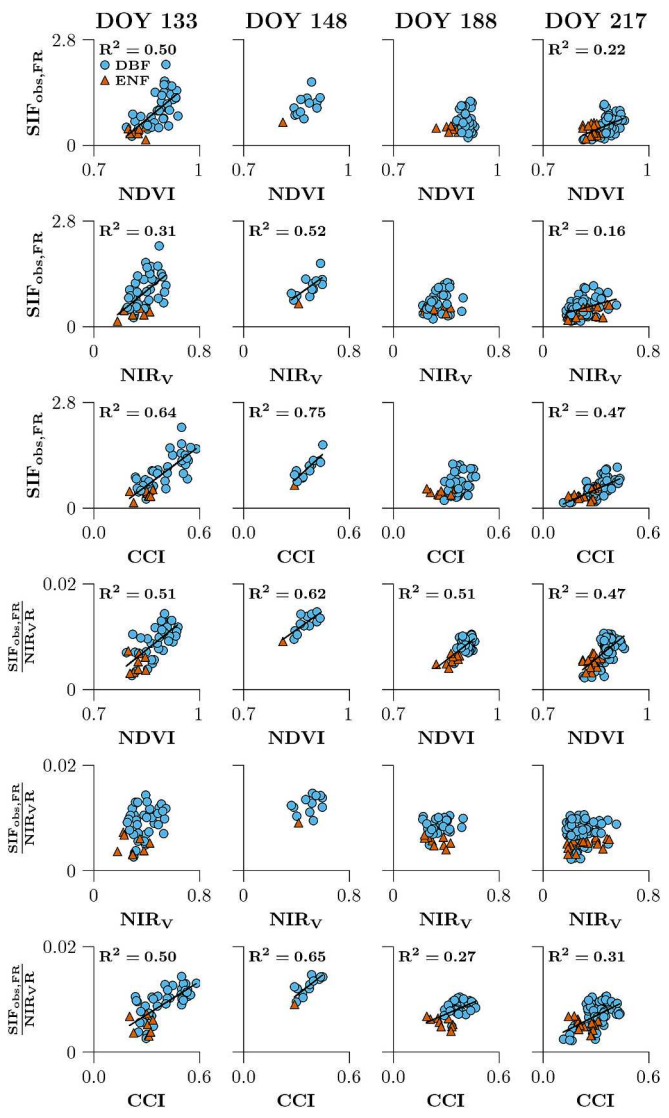

Fig. 5. Scatterplots of canopy NDVI, NIR_V, and CCI, against $SIF_{obs,FR}$ (mW m^{-2} sr^{-1} nm^{-1}) and $\frac{SIF_{obs,FR}}{NIR_VR}$, for the peak growing season dataset. Each column represents a week where FluoSpecAir was flown, with the day of year (DOY) displayed at the top of the column. Data across all hourly intervals (7:00–16:00) are shown. The linear regression lines for significant relationships (Bonferroni adjusted $P \leq 0.008$) are shown in black, with the corresponding coefficient of determination (R^2) displayed in the upper left.

3.2. Relationships between LAD parameters and remote sensing observations

For full results of our exploratory analysis on interpreting beta distribution parameters, we refer readers to Appendix A. However, we identified several important points about ν and μ. First, ν and μ are inversely related to variance – lower values indicate greater variability in leaf angle while higher values indicate low variability. Furthermore, when the mean leaf angle is greater than 45°, as is the case for all canopies in this study (Table S1), ν and μ have specific interpretations; 1) ν is mainly affected by the variance in leaf angle (Fig. A1); 2) μ is sensitive to both the mean and variance of leaf angle (Fig. A1), and is conceptualized as the variance in leaf angle when controlling for the effects of mean angle on the variance (Fig. A4) – as leaf angles are constrained from 0° to 90°, mathematically, variation in angle must be relatively lower the closer distribution mean is to either extreme. Another noteworthy point arising from the calculation of ν and μ is that when the mean leaf angle is greater than 45°, ν will be larger than μ, with the opposite being true at mean leaf angles lower than 45°.

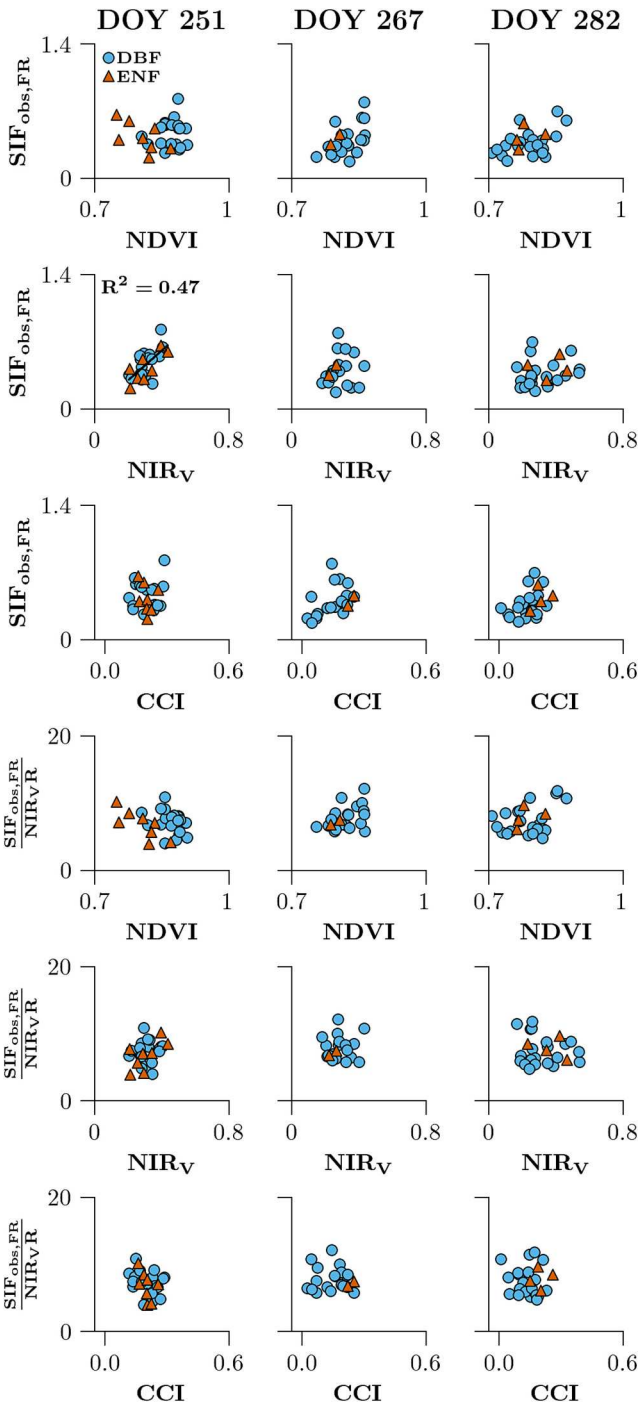

Fig. 6. Scatterplots of canopy NDVI, NIR_V, and CCI, against $SIF_{obs,FR}$ (mW m^{-2} sr^{-1} nm^{-1}) and $\frac{SIF_{obs,FR}}{NIR_VR}$, for the foliar senescence dataset. Each column represents a week where FluoSpecAir was flown, with the day of year (DOY) displayed at the top of the column. Data across all hourly intervals (7:00–16:00) are shown. The linear regression lines for significant relationships (Bonferroni adjusted $P \leq 0.008$) are shown in black, with the corresponding coefficient of determination (R^2) displayed in the upper left.

In the peak growing season, we observed a negative relationship between beta distribution parameters and remote sensing variables, indicating that canopies with greater variation in leaf angle had larger canopy NDVI, CCI, $SIF_{obs,FR}$, and $\frac{SIF_{obs,FR}}{NIR_VR}$ (Fig. 7). We did not find any

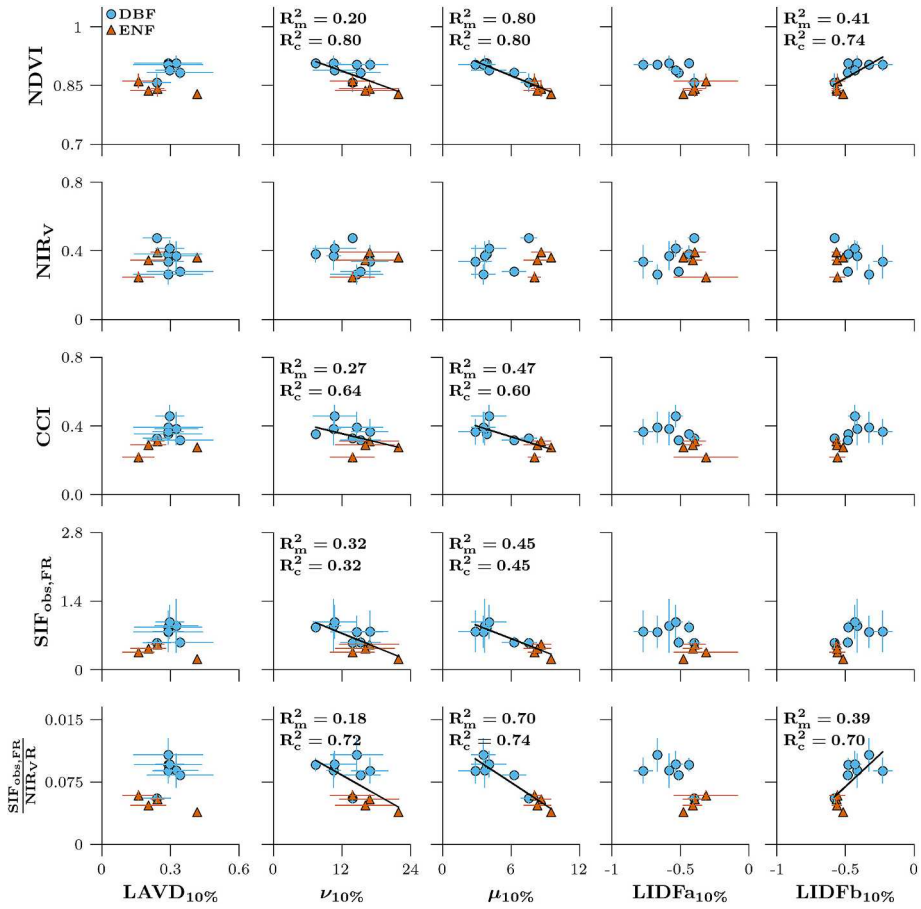

Fig. 7. Spatial relationships between $LAVD_{10\%}$ ($m^2\ m^{-3}$), leaf angle distribution parameters from the beta distribution ($\nu_{10\%}$, $\mu_{10\%}$), and LIDF distribution ($LIDFa_{10\%}$, and $LIDFb_{10\%}$), and canopy NDVI, NIR_V, CCI, $SIF_{obs,FR}$ ($mW\ m^{-2}\ sr^{-1}\ nm^{-1}$), and $\frac{SIF_{obs,FR}}{NIR_VR}$, for the peak growing season. We show the "between-group" associations from our linear mixed models, where each data point is the mean value for each canopy ($n = 11$) across all weeks of measurements (see Table 1). The error bars represent one standard deviation. The R^2_m (marginal R^2) and R^2_c (conditional R^2) for each significant linear-mixed model (Bonferroni adjusted $P \leq 0.002$) are displayed in the upper left.

significant models between LAVD and our remote sensing variables, or for models using beta distribution LAD parameters and canopy NIR_V. Linear mixed models using $\nu_{10\%}$ or $\mu_{10\%}$ produced similar a R^2_c, but differed considerably in their values of R^2_m, which is the proportion of variance explained by the fixed (i.e. $\nu_{10\%}$ or $\mu_{10\%}$) effect only. Models using $\mu_{10\%}$ had a larger R^2_m and a smaller difference between R^2_c and R^2_m, compared to $\nu_{10\%}$. Canopy NDVI and $\frac{SIF_{obs,FR}}{NIR_VR}$ had the strongest relationships with $\nu_{10\%}$ and $\mu_{10\%}$, with $R^2_c \geq 0.75$. The fixed effect of $\mu_{10\%}$ accounted for 80 % and 73 % of the variation in canopy NDVI and $\frac{SIF_{obs,FR}}{NIR_VR}$. No significant models were generated using $LIDFa_{10\%}$ as a predictor variable, while $LIDFb_{10\%}$ was positively related to canopy NDVI and $\frac{SIF_{obs,FR}}{NIR_VR}$. R^2_c values for $LIDFb_{10\%}$ were lower compared to $\nu_{10\%}$ and $\mu_{10\%}$, while R^2_m values were in-between $\nu_{10\%}$ and $\mu_{10\%}$. No significant models were found using $LAVD_{10\%}$, though we note that one ENF canopy (red pine, ID 30) had a large $LAVD_{10\%}$ while its LAD parameters were consistent with other ENF canopies.

When examining relationships in the foliar senescence dataset, we did not observe any significant relationships (Fig. S7). However, models using $\mu_{10\%}$ and LIDFb were trending significant ($P \leq 0.05$) for canopy NDVI and $\frac{SIF_{obs,FR}}{NIR_VR}$. Relationships with mean and SD leaf angle varied between the two datasets (Figs. S8, S9). In the peak growing season, models using $SD_{10\%}$ were trending significant for all remote sensing variables (Fig. S8). In the foliar senescence dataset, $mean_{10\%}$ was trending significant for canopy NDVI and NIR_V (Fig. S9), with $mean_{10\%}$ being positively related to canopy NDVI and negatively related to NIR_V. Beta distribution parameter μ was highly related to LIDFb ($R^2 \geq 0.90$, not shown), while the relationship between LIDFa and mean leaf angle was nearly a perfect line ($R^2 \geq 0.98$ not shown).

3.3. Relationships between remote sensing metrics and leaf chlorophyll content

PROSPECT-D inversions were able to accurately replicate our measurements of leaf reflectance spectra using a leaf clip (Fig. S10) from 400 nm – 950 nm. When comparing the measured reflectance spectra to the simulated, we report a median root mean square error (RMSE) and standard error of 0.0086 ± 0.0004. During the peak growing season, leaf chlorophyll content ranged from 52 to 86 μg cm^2 with a median and standard deviation of 67 ± 9. During the foliar senescence dataset, leaf chlorophyll content ranged from 35 to 78 μg cm^2 with a median and standard deviation of 53 ± 13. When correlating leaf chlorophyll content to midday observations of $\frac{SIF_{obs,FR}}{NIR_VR}$ for a given sampling week, we found positive relationships between both variables for both datasets (Fig. 8). While we did not see significant relationships between leaf chlorophyll content and $LAVD_{100\%}$ and $\mu_{100\%}$ (data not shown), we observe a negative relationship with $\nu_{100\%}$ for both datasets (Fig. 9).

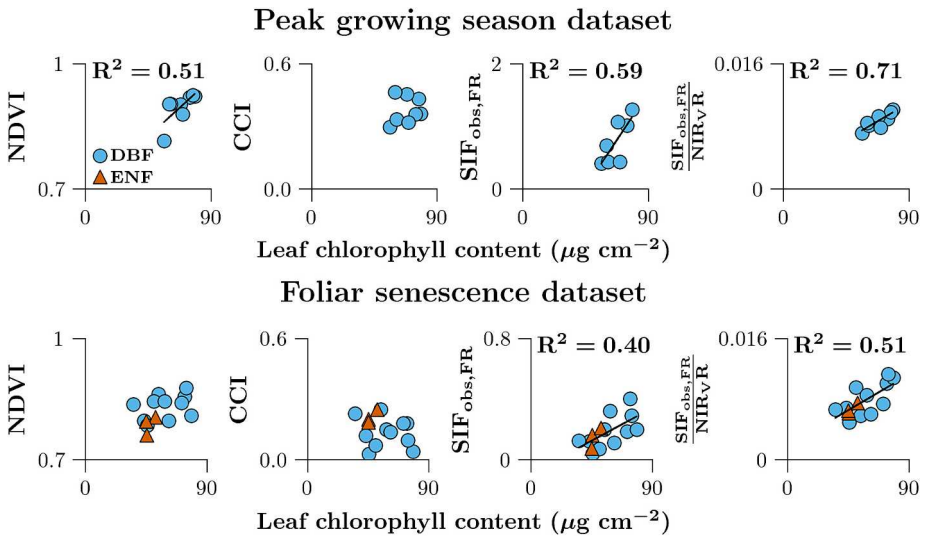

Fig. 8. Relationships between leaf chlorophyll content and canopy NDVI, CCI, $SIF_{obs,FR}$ (mW m^{-2} sr^{-1} nm^{-1}), and $\frac{SIF_{obs,FR}}{NIR_VR}$, for the peak growing season ($n = 8$) and foliar senescence ($n = 14$) datasets. No ENF canopies were sampled during the peak growing season. The linear regression lines for significant relationships (Bonferroni adjusted $P \leq 0.05$) are shown in black, with the corresponding coefficient of determination (R^2) displayed in the upper left.

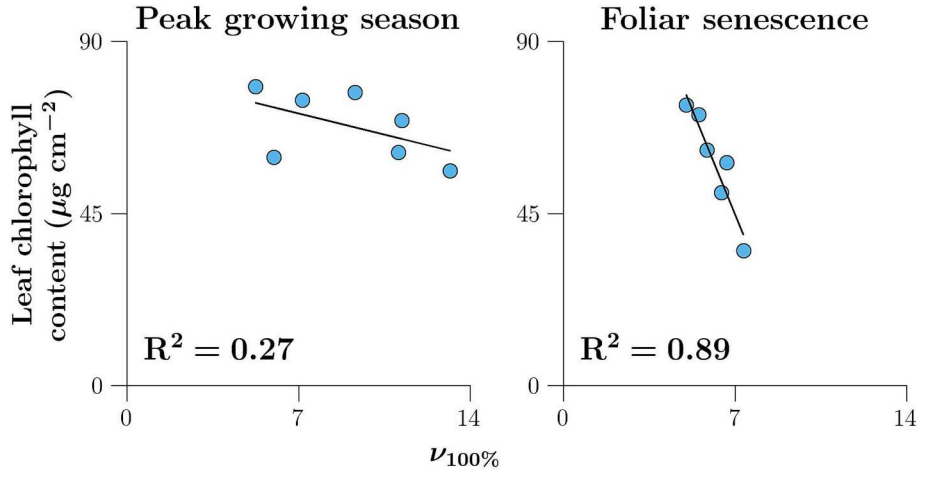

Fig. 9. The relationship between $\nu_{100\%}$ and leaf chlorophyll content for DBF canopies in the peak growing season ($n = 7$) and foliar senescence ($n = 6$) datasets. The number of points for each dataset is smaller than in Fig. 8 due to TLS data being unavailable for some canopies. Solid black lines are the linear regressions, with the coefficient of determination (R^2) displayed in the lower left.

3.4. Assessing the relationship between $\frac{SIF_{obs,FR}}{NIR_VR}$ and $\phi_{F,FR}$

When we tested the assumption that $\frac{SIF_{obs,FR}}{NIR_VR}$ is proportional to $\phi_{F,FR}$, we did not see any apparent relationship between $\frac{SIF_{obs,FR}}{NIR_VR}$, $\frac{PAR}{S_{NIR}}$, and $\frac{1-\omega_{PAR}}{\omega_{NIR}}$ (Fig. S11). $\frac{1-\omega_{PAR}}{\omega_{NIR}}$ exhibited little variation among DBF canopies in both datasets. There was a difference in $\frac{1-\omega_{PAR}}{\omega_{NIR}}$ when comparing DBF vs ENF canopies in the foliar senesce dataset, with ENF canopies having a $\frac{1-\omega_{PAR}}{\omega_{NIR}}$ around 0.9, while DBF species were around 1 (Fig. S11). No ENF canopies were sampled for the peak growing season dataset. $\frac{PAR}{S_{NIR}}$ varied more within the foliar senescence dataset (Fig. S11) compared to the peak growing season data, but overall, variation in $\frac{PAR}{S_{NIR}}$ was low. Furthermore, for any given flight, all remote sensing observations are made within ~10 min each other, thus $\frac{PAR}{S_{NIR}}$ should not vary significantly. As our analyses in Figs. 4–9 are separated by individual weeks, variation in $\frac{PAR}{S_{NIR}}$ should will be minimal. Based on these results, we concluded that variability in $\frac{SIF_{obs,FR}}{NIR_VR}$ is driven primarily by differences in $\phi_{F,FR}$ across the peak growing season dataset.

4. Discussion

4.1. Coordination between function and structure drive remote sensing relationships

Our results show that during the peak growing season, canopies exhibiting greater variation in leaf angle have a larger NDVI, CCI, $SIF_{obs,FR}$, and $\frac{SIF_{obs,FR}}{NIR_VR}$ (Fig. 7), and they have higher leaf chlorophyll content (Fig. 9). We attribute this finding to the coordination between canopy function and structure – assemblages of biochemical and structural traits are coordinated to facilitate a particular growth strategy (McNeil et al., 2023; Reich, 2014). We propose that increasing intra-canopy leaf angle variability enhances light interception in the visible wavelengths, allowing canopies to invest in greater concentrations of foliar pigments.

The exact configurations of leaf placement within a canopy that leads to increased variability in leaf angle and enhanced light interception are unknown, but this could be addressed in future studies using 3D radiative transfer models (Gastellu-Etchegorry et al., 2017). As we discuss further on in Section 4.2., the radiative transfer mechanisms driving the strong coupling between LAD and our remote sensing variables likely include factors beyond the relationship between LAD and leaf chlorophyll content. Furthermore, the relationships in Fig. 7 were strengthened by a separation between DBF and ENF canopies, particularly with respect to LAD parameters. ENF canopies are known to be biochemically and spectrally distinct from DBF canopies – consistent with our understanding of plant strategies (Guillén-Escribà et al., 2021; Lusk et al., 2003; Serbin et al., 2014). Our data suggest that DBF and ENF canopies also differ in their LAD, although to what degree DBF and ENF species might overlap in their range of LAD values remains to be seen. However, given sufficient sample sizes for each, we would still expect comparable relationships within each PFT when comparing LAD with the same remote sensing variables.

Enhanced light interception increases whole-canopy photosynthesis, and the positive covariation of $\frac{SIF_{obs,FR}}{NIR_VR}$ with leaf chlorophyll and LAD may be indicative of these larger photosynthetic rates. Model simulations have shown that the fluorescence yield increases with photosynthetic capacity under light-saturating conditions (Johnson and Berry, 2021). The model results in Johnson and Berry (2021) are also consistent with the positive correlation between leaf chlorophyll and $\frac{SIF_{obs,FR}}{NIR_VR}$ observed in our data (Fig. 8). Furthermore, leaf chlorophyll content is positively related to foliar nitrogen and photosynthetic capacity (Croft et al., 2017) in some DBF species, including red maple, which we measured in our study. Thus, an exciting implication is that our remote sensing data are capturing differences in whole-canopy photosynthesis among individual tree canopies, although we do not have measurements of leaf gas exchange or foliar nitrogen to confirm this.

One curiosity is that our data showed a stronger relationship between canopy NDVI and $SIF_{obs,FR}$ compared to canopy NIR_V (Fig. 5). This is surprising, as empirical studies and RTM simulations have shown a strong relationship between SIF and NIR_V (Badgley et al., 2017; Du et al., 2023; Zeng et al., 2019). The reasons for this discrepancy are unclear, but one possibility merits discussion. Prior studies showed a strong coupling between NIR_V and SIF from coarse spatiotemporal resolutions (Badgley et al., 2017) or stationary tower observations from a fixed FOV across ecosystems (Du et al., 2023), while our study examines relationships at a previously unstudied spatiotemporal scale of individual tree canopies at hourly intervals. This may suggest that scaling affects the relationship between NIR_V and SIF – a phenomenon that has been previously reported in Arctic Boreal vegetation using 30 m^2 airborne imagery (Maguire et al., 2021). Similar to Maguire et al. (2021), our results may indicate that spatial variability in canopy $SIF_{obs,FR}$ is driven more by leaf chlorophyll than canopy structure, as NDVI is sensitive to chlorophyll and canopy structure, while NIR_V is primarily sensitive to canopy structure. The correlations of $SIF_{obs,FR}$ with leaf chlorophyll content (Fig. 8) and canopy CCI (Fig. 5) are consistent with this view as well. Our data can also contradict this hypothesis, as notably NIR_V was more strongly coupled with $SIF_{obs,FR}$ than NDVI in our foliar senescence dataset on DOY 251, and perhaps suggests potential measurement uncertainties associated with our FluoSpecAir system. Future studies that explicitly address questions of scaling with remote sensing observations may be able to definitively resolve this particular finding.

Leaf chlorophyll content is also a strong driver of $\frac{SIF_{obs,FR}}{NIR_VR}$ in our study. It was previously shown that when using $NIR_v \times PAR$ (NIR_VP), $\frac{SIF_{obs,FR}}{NIR_VP}$ and canopy CCI are tightly coupled seasonally in a boreal ENF forest (Kim et al., 2021). Surprisingly, in our data, we found that canopy NDVI had roughly comparable, or stronger, correlations with $\frac{SIF_{obs,FR}}{NIR_VR}$ compared to canopy CCI. This is a novel finding within our dataset, and could be related to canopy NDVI acting as a better indicator of photosynthetic capacity than CCI. In our data, the influence of chlorophyll on NDVI, as well as the indirect effect of foliar nitrogen on NIR albedo (Knyazikhin et al., 2013; Townsend et al., 2013), could lead to the stronger relationship with $\frac{SIF_{obs,FR}}{NIR_VR}$. However, we caution that additional field studies are needed to verify the connections between canopy NDVI, $\frac{SIF_{obs,FR}}{NIR_VR}$, and photosynthetic capacity.

4.2. The direct and indirect effects of LAD on remote sensing observations

Here, we distinguish the effects of LAD, and canopy structural traits more broadly, on remote sensing observations as both direct and indirect. The direct effects relate to how canopy structural traits impact radiative transfer properties such as $i_{0,green}$ and $f^{esc}_{(\lambda,\Omega)}$. The indirect effects of canopy structural traits are related to the coordination between function and structure. In our study, we found that within-canopy variability in leaf angle is more strongly related to our remote sensing observations than the mean leaf angle of the canopy (Fig. 7, Fig. S7 – S9). As we discussed in 4.1., this appears to be an indirect effect that is predicated on the relationship between LAD and leaf chlorophyll (Fig. 9). However, within-canopy variability in LAD should also affect $i_{0,green}$ and $f^{esc}_{(\lambda,\Omega)}$ as well, and these factors are likely to be contributing to the strength of the relationships in Fig. 7. This can be reasoned by observing that the relationships between LAD and our remote sensing variables are considerably stronger compared to the relationships with leaf chlorophyll content, and the relationship between LAD and leaf chlorophyll content. Thus, changes in $i_{0,green}$ and $f^{esc}_{(\lambda,\Omega)}$ as LAD changes, are likely contributing additional explanatory power – however this would need to be more thoroughly investigated using RTM simulation.

Our findings are contrasted with RTM-based studies, which have illustrated the direct effects of mean leaf angle on canopy reflectance (Hase et al., 2022; Jacquemoud et al., 2009; Kattenborn et al., 2024; Zeng et al., 2019). Our results are not inconsistent with RTM simulations however – we observed a negative relationship between mean leaf angle and canopy NIR_V (Fig. S9) that mirrors studies using RTM simulations (Kattenborn et al., 2024; Zeng et al., 2019). In other instances, relationships among remote sensing variables with mean leaf angle were not significant, but small sample sizes are limiting our power (Fig. S8). We also stress that our understanding of the direct effects of LAD on radiative transfer, particularly within complex canopies such as forests, is incomplete and limited, partly due to a lack of observational data. For example, no RTM-based studies have examined how canopy variability in leaf angle affects $i_{0,green} \times f^{esc}_{(\lambda,\Omega)}$, and resulting observations of reflectance and SIF. Thus, while it may be surprising that our dataset shows a much stronger relationship between parameters of leaf angle variability and remote sensing observations compared to the mean leaf angle, our findings are within reason.

We also found the relationship between LAD and canopy NDVI to be appreciably stronger than the relationship between LAD and canopy CCI. This is likely because canopy CCI was designed to measure the relative concentrations of chlorophyll to carotenoids (Gamon et al., 2016). In-situ field observations have shown positive relationships between total-chlorophylls and canopy CCI (Wong et al., 2020), but our own data did not corroborate this finding (Fig. 8). However, the relationship between chlorophyll and canopy CCI found by Wong et al. (2020) were species dependent. The limited number of individuals per species in our study may prevent a clearer relationship from being present in our dataset. Furthermore, given the consistent pattern between LAD, canopy NDVI, and canopy CCI, and canopy NDVI and canopy CCI with SIF and $\frac{SIF_{obs,FR}}{NIR_VR}$, we believe it is still reasonable to assume larger CCI values correspond to a greater leaf chlorophyll content in our data.

4.3. Phenological stage affects coordination between function and structure

While our peak growing season data showed coordination between function and structure, data collected during foliar senescence (2020) showed no significant relationships among our remote sensing variables (Fig. 6, Fig. S7). This result is not unexpected, as the main physiological function of plants during this time is remobilization and reallocation of nutrients in preparation for growth during the following spring rather than resource acquisition at that moment (Chapin, 1980; Killingbeck, 1996). This process is characterized by the breakdown of chlorophyll and leaf proteins (Christ and Hörtensteiner, 2014; Hörtensteiner and Feller, 2002; Kuai et al., 2018), resulting in the decline and eventual termination of photosynthetic processes, including leaf gas exchange and ϕ_{PSII} (McConnaughay et al., 1996; Weng et al., 2005). These changes in leaf biochemistry affect spectral reflectance, which we observed in our FluoSpecAir data (Fig. 4.). The onset of senescence creating changes in leaf optical properties and photosynthesis likely explains why canopy CCI and canopy NDVI were not correlated with $SIF_{obs,FR}$ or $\frac{SIF_{obs,FR}}{NIR_VR}$ in the foliar senescence dataset (Fig. 6). We also attribute the lower values of $SIF_{obs,FR}$ observed in the foliar senescence dataset (Fig. 4d) to functional changes more than structural ones. The physiological breakdown of chlorophyll will reduce APAR, leading to lower values of $SIF_{obs,FR}$. Additionally, we observed lower values of $\frac{SIF_{obs,FR}}{NIR_VR}$ (Fig. 4e), indicating that $\phi_{F,\lambda}$ was also lower during this time period, which would also contribute to lower values of $SIF_{obs,FR}$. Canopy structural metrics however remained comparatively stable between the two datasets (Fig. 4f – 4h, Fig. S4f, S4g), further pointing to functional changes driving the lower values in $SIF_{obs,FR}$.

Despite the lack of relationships with SIF variables from either remote sensing indices or LAD, we still observed positive relationships between leaf chlorophyll content, SIF, and $\frac{SIF_{obs,FR}}{NIR_VR}$ (Fig. 8). Our foliar sampling preferentially selected non-chlorotic leaves and tissues for spectral measurements, as senescing leaves would have a significantly reduced SIF emission. As the canopy SIF emission would predominantly be from the remaining green vegetation, it is unsurprising to see correlations between leaf chlorophyll and SIF variables. From a statistical perspective, there is an even stronger decoupling between leaf chlorophyll and $SIF_{obs,FR}$ in the foliar senescence dataset. Compared to the peak growing season, leaf chlorophyll content had a larger range and was more variable, while $SIF_{obs,FR}$ was less variable with a smaller range. While the greater variability in leaf chlorophyll content should lead to stronger correlations, we find a weaker R^2 with $SIF_{obs,FR}$ – in part due to the smaller range and variability of $SIF_{obs,FR}$.

4.4. $\frac{SIF_{obs,FR}}{NIR_VR}$ is a proxy for $\phi_{F,\lambda}$

As indicated by Eq. 8, the constitutive components of $\frac{SIF_{obs,FR}}{NIR_VR}$ are related to the light environment ($\frac{PAR}{S_{NIR}}$), leaf albedo ($\frac{1-\omega_{PAR}}{\omega_{NIR}}$), and $\phi_{F,\lambda}$. As we observed no relationship between $\frac{SIF_{obs,FR}}{NIR_VR}$ and the light environment or leaf albedo terms (Fig. S11), our conclusion was that $\frac{SIF_{obs,FR}}{NIR_VR} \approx \phi_{F,FR}$. However, we were unable to make leaf-level measurements of ϕ_F to compare against $\frac{SIF_{obs,FR}}{NIR_VR}$, preventing us from making a definitively validating the approach suggested by Zeng et al. (2022). There are also several assumptions and uncertainties using this method that merit discussion. First, this method is slightly sensitive to soil background brightness (Zeng et al., 2022), although we note that all FluoSpecAir measurements completely covered each tree canopy – minimizing the contribution of soil background. Another noteworthy point is that the ENF and DBF leaves exhibited separation in the $\frac{1-\omega_{PAR}}{\omega_{NIR}}$ term, suggesting that neither ω_{PAR} or ω_{NIR} should be assumed to be constant across plant functional types. Lastly, acknowledge the possibility that $\frac{SIF_{obs,FR}}{NIR_VR}$ could show no correlation with $\frac{PAR}{S_{NIR}}$, $\frac{1-\omega_{PAR}}{\omega_{NIR}}$, or ϕ_F, while still showing a correlation between the product of the three.

4.5. The potential influence of clumping index

While TLS processing algorithms are rapidly advancing, it should be noted that no methods exist to estimate the clumping index of individual trees from TLS. Canopy clumping, which describes the spatial deviation of foliage with respect to a random distribution (Nilson, 1971), is a critical structural parameter and is essential for understanding canopy radiative transfer processes. Contemporary methods rely on using the entire TLS scan to derive a plot level estimate of clumping index (Ma et al., 2018; Schraik et al., 2023). While clumping index is known to vary by species, there is some limited evidence suggesting that clumping covaries vertically with leaf angle (Béland and Baldocchi, 2020). Thus, it's possible that our relationships between LAD and remote sensing observations include some effects of clumping index.

4.6. Leaf angle distribution – contextualizing our measurements

Our study is one of a handful of studies that have quantified the LAD of tree crowns from multiple species with TLS. Most studies that report LAD rely on a leveled digital photography method (Chianucci et al., 2018; Pisek et al., 2022; Raabe et al., 2015) which is more labor and time intensive, and cannot measure whole canopies. Despite these drawbacks, these approaches yield comparable results to TLS-derived methods (see Kattenborn et al., 2022; Pisek et al., 2022). When comparing LAD from our deciduous broadleaf species, we observed higher mean values of leaf angle, and lower standard deviations in leaf angle in *Acer rubrum* and *Prunus serotina* compared to other species in their respective genus (Table S1, Pisek et al., 2022). Values of ν are also larger in our data, while μ falls within reported ranges for comparable species. LAD reported in Pisek et al. (2022), the most comprehensive dataset available, predominantly comes from European trees. There are considerable differences in environment and latitude with our data collected in the mid-Atlantic region of the U.S. Thus, we would expect to observe differences in mean angle and beta parameters.

4.7. Leaf angle distribution – reporting and choice of parameters matter

It is important to report a suite of parameters related to LAD as they are important for the remote sensing and forest structure communities. Tabular data reporting means, standard deviation, ν, and μ, are relatively scarce and should be standard output for future studies that quantify LAD. These metrics are important because of their strong tie with remote sensing observations (Figs. 7, 8). Studies often assign observed LAD to a "best-fit" theoretical LAD (e.g., plagiophile, Raabe et al., 2015), but variation in LAD falls along a gradient that has no clear boundaries between these types. We also suggest that, when possible, the vertical profile of these values should be provided. Additionally, the choice of distribution parameters (i.e., beta distribution, LIDF, or mean and standard deviation) matters. RTMs such as SCOPE rely on LIDF, which is parameterized by LIDFa and LIDFb. However, the LIDF produces leaf angle distributions that are different compared to those based on beta distribution parameters. We observed this in our observational data (Fig. S12) and when replicating theoretical leaf angle distributions (e.g., spherical, plagiophile, etc., Fig. S13). When using the LIDF, the leaf angle distribution was overestimated at the tails, whereas the beta distribution underestimated the peak (Fig. S12). Furthermore, the beta distribution fit to observational data better than the LIDF, with an average NRMSE of 6.4 % and 10.9 %, respectively. Given these points, including beta distributions as an alternative to LIDF parameters in

RTMs would allow for LAD to be more realistically represented, potentially creating more accurate model output. LIDF parameters are still useful however, particularly as their meaning is more interpretable than beta distribution parameters (e.g. LIDFa is closely related to mean leaf angle).

5. Conclusion

We used a novel remote sensing platform to study the spatial variability in SIF and canopy reflectance across two phenological periods (foliar senescence in 2020, the peak growing season in 2021). These remote sensing measurements were combined with TLS and foliar sampling to examine how functional and structural attributes of plant canopies spatially covary. Our study is the first to examine the empirical relationships between LAD, SIF, canopy reflectance indices, leaf chlorophyll content. Across the peak growing season, LAD parameters ν and μ were negatively related to canopy NDVI, CCI, SIF, $\frac{SIF_{obs,FR}}{NIR_VR}$ (Fig. 7, Fig. S3), and ν was negatively related to leaf chlorophyll content (Fig. 9). Canopy NDVI and CCI were also positively related with SIF and $\frac{SIF_{obs,FR}}{NIR_VR}$ (Fig. 5). Our results highlight that canopies with greater variation in leaf angle have more chlorophyll and larger remote sensing values, as ν and μ are inversely related to variance in leaf angle (Fig. A1). These findings are consistent with ecological principles regarding coordination between canopy function and structure. We hypothesize that greater intra-canopy variation in leaf angle enhances light interception, driving a demand for greater allocation of foliar resources and enhancing whole-canopy photosynthesis. We also found that parameters from the beta distribution fit to real world distributions of leaf angle better than LIDF parameters, which are commonly used in radiative transfer models. Our results illustrate the importance of direct versus indirect effects of canopy structure when interpreting spatial variability in canopy reflectance and SIF across a landscape.

CRediT authorship contribution statement

Andrew D. Jablonski: Writing – review & editing, Writing – original draft, Investigation, Formal analysis, Data curation, Conceptualization. **Rong Li:** Writing – review & editing, Conceptualization. **Jongmin Kim:** Writing – review & editing, Conceptualization. **Manuel Lerdau:** Writing – review & editing, Conceptualization. **Carmen Petras:** Data curation. **Xi Yang:** Writing – review & editing, Resources, Funding acquisition, Conceptualization.

Declaration of competing interest

The authors declare that they have no known competing financial interests or personal relationships that could have appeared to influence the work reported in this paper.

Acknowledgements

This work was supported by the National Science Foundation (IOS-200554 and DEB-2405619). XY and AJ acknowledge the support from The Future Investigators in NASA Earth and Space Science and Technology from the National Aeronautics and Space Administration (80NSSC20K1653). RL and XY acknowledge support from The Future Investigators in NASA Earth and Space Science and Technology from the National Aeronautics and Space Administration (80NSSC22K1297).

Appendix A. Interpreting beta distribution parameters ν and μ

Using a beta distribution, the probability density function for leaf angle (θ_L) distribution is calculated as,

$$f(t) = \frac{1}{B(\nu,\mu)}(1-t)^{\mu-1}t^{\nu-1} \tag{A1}$$

where $t = 2\theta_L/\pi$ and $B(\nu,\mu) = (\Gamma(\nu)\Gamma(\mu))/(\Gamma(\nu+\mu))$, where Γ is the gamma function. Parameters ν and μ are related to the mean ($\bar{t}$) and variance (σ^2) of leaf angle distribution through the equations,

$$\nu = \bar{t}\left(\frac{\sigma_0^2}{\sigma^2} - 1\right) \tag{A2}$$

$$\mu = (1-\bar{t})\left(\frac{\sigma_0^2}{\sigma^2} - 1\right) \tag{A3}$$

with σ_0^2 representing the maximum variance, calculated as $\sigma_0^2 = \bar{t}(1-\bar{t})$. Effectively, ν and μ incorporate the mean and variability of t, and are complements, with their sum being equal to the concentration $\left(\frac{\sigma_0^2}{\sigma^2} - 1\right)$. To better understand the biophysical interpretation of ν and μ, we performed an exploratory analysis using simulated data and our in-situ observations from all TLS data collected in this study.

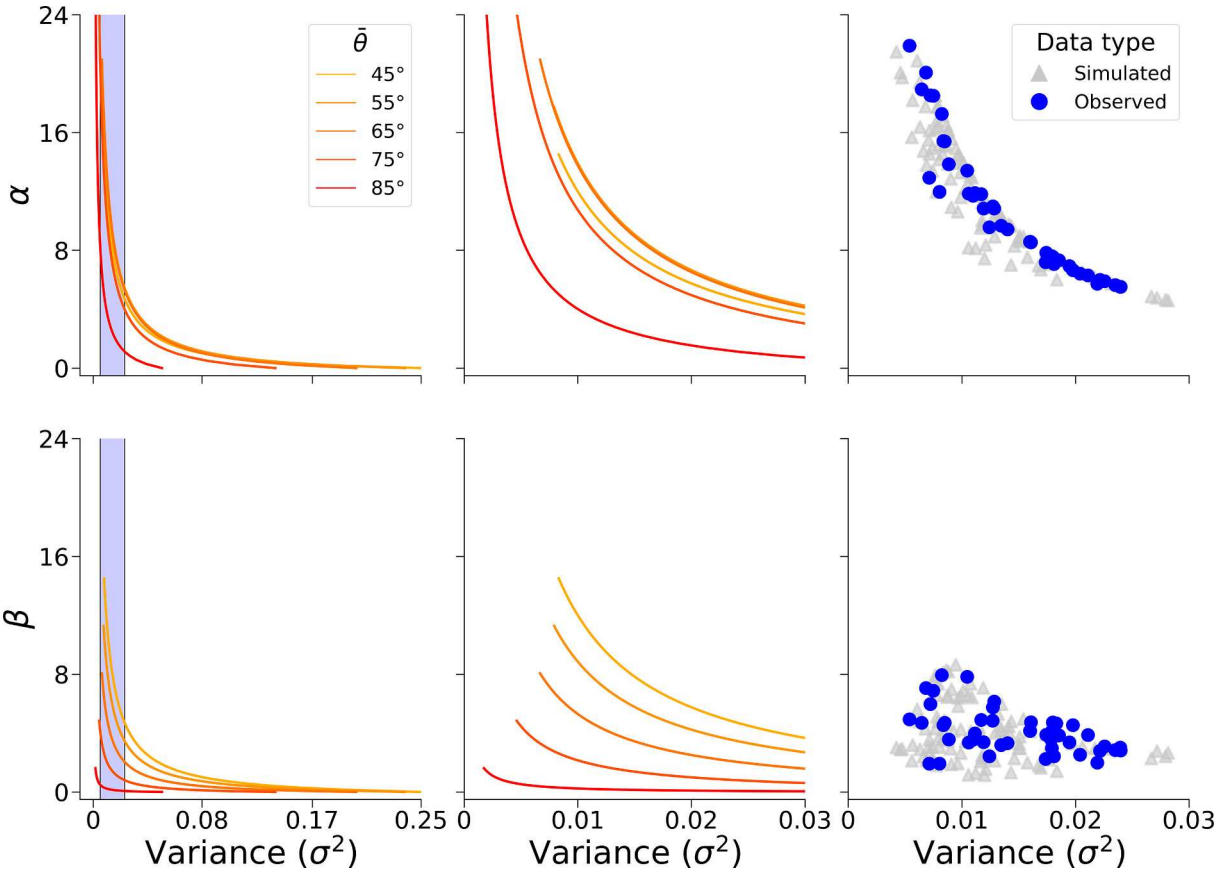

Fig. A1. First column: The relationship between σ^2 and beta distribution parameters ν and μ at five different mean values, starting from 45° and increasing in increments of 10°. The blue shaded region represents the range of σ^2 observed from our empirical data. Second column: The same plot as the first column, but the range of σ^2 is constrained to the blue shaded region in the first column. Third column: Scatterplots between σ^2 and ν and μ using empirical data from this study (blue dots), and simulated data (light gray triangles). (For interpretation of the references to colour in this figure legend, the reader is referred to the web version of this article.)

First, we examined how σ^2 is related to ν and μ at five different values of $\bar{t}$ ($\bar{\theta}_L = 45°, 55°, 65°, 75°, 85°$, first two columns of Fig. A1.). While the overall curvature of the relationship between σ^2 and ν and μ is similar across different means, the relationship between σ^2 and μ is more affected by $\bar{t}$, particularly in the range of our in-situ observations (shaded rectangle in the first column, the middle column shows the relationship within the constraints of our observed data). As a result, our in-situ observations between σ^2 and ν show a strong relationship (top rightmost panel, blue circles), while σ^2 and μ show considerably more scatter (bottom rightmost panel, blue circles). To check these relationships, we simulated 100 random points constrained by the observed values of $\bar{t}$ and the concentration, and overlayed those points with our in-situ observations (rightmost panels, gray triangles). The patterns from our simulated data track with our in-situ data. As the relationship between σ^2 and μ is poor, simplifying the interpretation of μ as σ^2 is largely incorrect. From Eq. A3, the concentration is likely a stronger driver of variation in μ. However, when checking the relationship between the concentration and μ, considerable scatter was still apparent (not shown, $r^2 = 0.59$). Thus, we explored further formulations to explain μ while retaining parsimony.

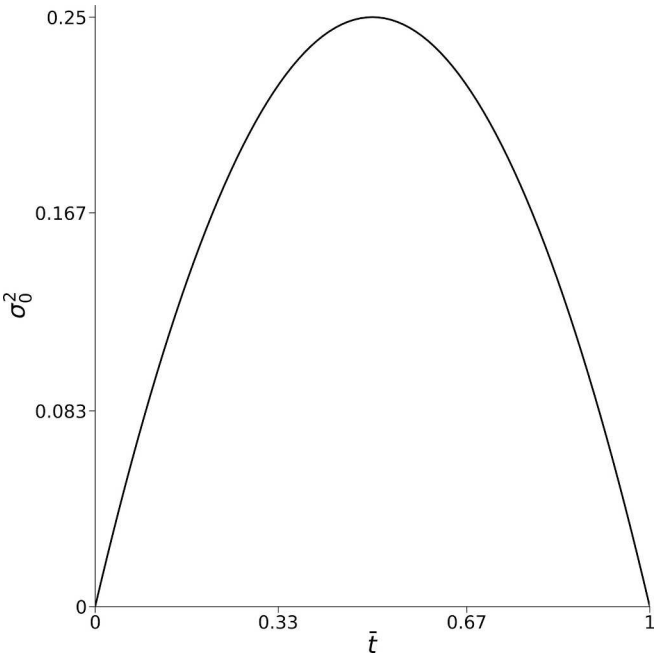

Fig. A2. The relationship between $\bar{t}$ and σ_0^2.

The concentration is the ratio between σ_0^2 and σ^2; conceptually it represents how much variation there is with respect to the maximum variance allowed for a given $\bar{t}$. This a purely a mathematical construct based on the beta transformation which restricts values between 0 and 1. When $\bar{t}$ approaches 0 or 1 ($\bar{\theta}_L = 0^\circ$ and 90° respectively) σ_0^2 decreases; variances larger than σ_0^2 would create values outside the bounds of 0 and 1. From Fig. A2, σ^2 is maximized at 45° – an interesting question arises as to the extent to which actual maximum variation in leaf angle tracks with this statistical constraint. We note the lowest observed value of concentration in our data was 7.7.

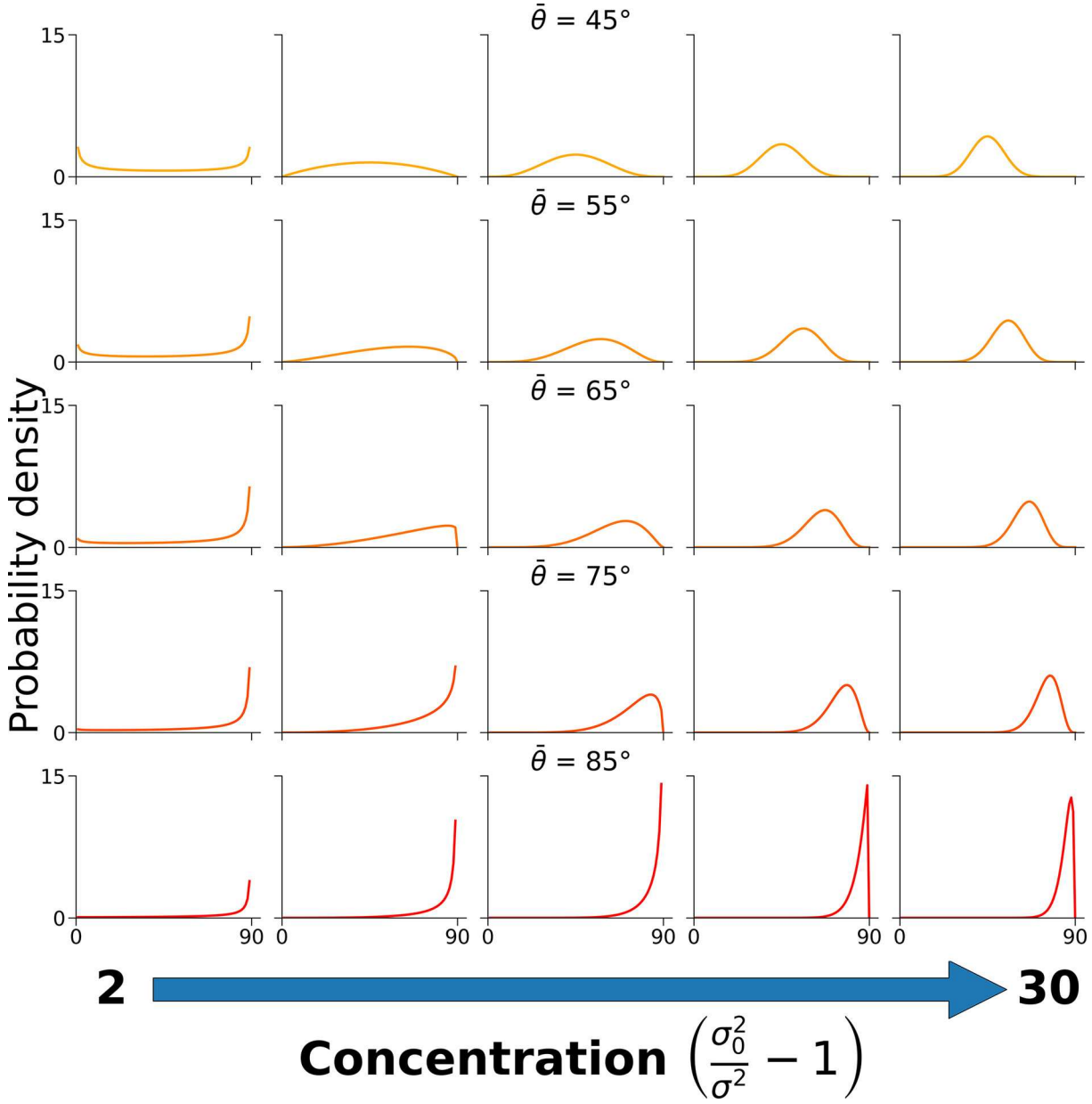

Fig. A3. Simulated leaf angle distributions under different values of concentration and mean leaf angle. From columns moving left to right, values of concentration increase, starting at a concentration of 2 and ending with a concentration of 30. From columns moving from top to bottom, mean leaf angle increases, starting at 45° and ending at 85°.

To visualize how variation in concentration affects leaf angle distribution at different levels of $\bar{t}$, we simulated leaf angle distributions with the same five $\bar{t}$ from before, while varying the concentration (from 2 to 30) at each value of $\bar{t}$. Lower values of concentration increase the spread of t, and as $\overline{\theta}_L$ approaches 45°, the spread of t becomes more uniform across all angles.

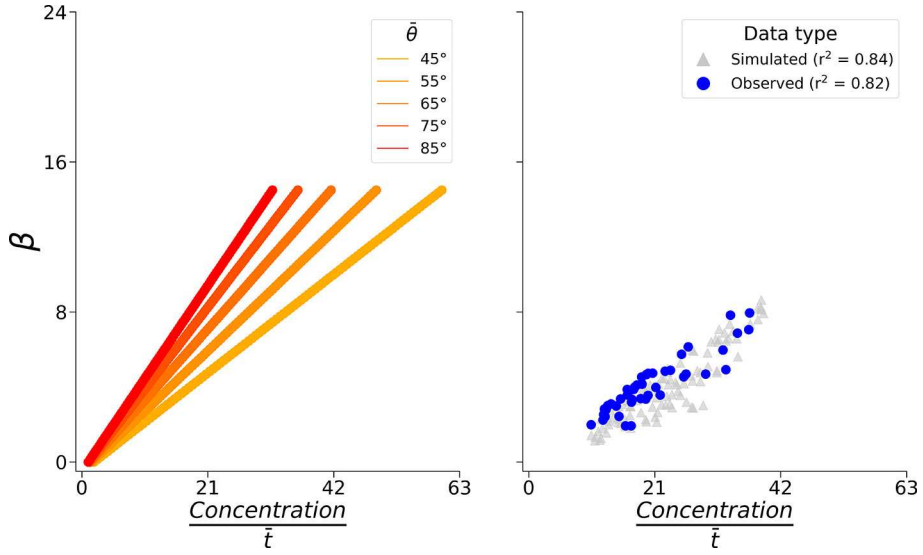

Fig. A4. Left panel: The relationship between the ratio of concentration to $\bar{t}$ and μ at five different mean values. Right panel: Scatterplots between the ratio of concentration to $\bar{t}$ and μ using empirical data from this study (blue dots), and simulated data (light gray triangles). (For interpretation of the references to colour in this figure legend, the reader is referred to the web version of this article.)

As the interaction between $\bar{t}$ and the concentration can change the shape of leaf angle distribution in both directions, we examined whether normalizing concentration by $\bar{t}$ would provide a greater contextualization of μ. While the slope of the relationship changes by $\overline{\theta}_L$ (left panel), deviation in the slopes gets smaller as $\overline{\theta}_L$ moves further away from 45°. This approximation tracks fairly well with our in-situ and simulated data (right panel) – low values of μ describe canopies that have greater variation in leaf angle when adjusting for some effects of $\overline{\theta}_L$. The effect of $\overline{\theta}_L$ isn't entirely removed, as the concentration contains the σ_0^2 term, which is governed by $\overline{\theta}_L$.

Appendix B. Supplementary data

Supplementary data to this article can be found online at https://doi.org/10.1016/j.rse.2025.114996.

Data availability

Field data, leaf spectra, canopy spectra, retrieved SIF, and leaf angle distribution data, will be made publicly available in the EcoSIS spectral repository (https://ecosis.org/) upon manuscript acceptance. Point cloud data from TLS will be made publicly available on the global TLS database (https://www.global-tls.net).

References

Ač, A., Malenovský, Z., Olejníčková, J., Gallé, A., Rascher, U., Mohammed, G., 2015. Meta-analysis assessing potential of steady-state chlorophyll fluorescence for remote sensing detection of plant water, temperature and nitrogen stress. Remote Sens. Environ. 168, 420–436. https://doi.org/10.1016/j.rse.2015.07.022.

Asner, G.P., 1998. Biophysical and biochemical sources of variability in canopy reflectance. Remote Sens. Environ. 64, 234–253. https://doi.org/10.1016/s0034-4257(98)00014-5.

Badgley, G., Field, C.B., Berry, J.A., 2017. Canopy near-infrared reflectance and terrestrial photosynthesis. Sci. Adv. 3, e1602244. https://doi.org/10.1126/sciadv.1602244.

Badgley, G., Anderegg, L.D.L., Berry, J.A., Field, C.B., 2019. Terrestrial gross primary production: using NIRV to scale from site to globe. Glob. Chang. Biol. 25, 3731–3740. https://doi.org/10.1111/gcb.14729.

Baldocchi, D.D., Ryu, Y., Dechant, B., Eichelmann, E., Hemes, K., Ma, S., Sanchez, C.R., Shortt, R., Szutu, D., Valach, A., Verfaillie, J., Badgley, G., Zeng, Y., Berry, J.A., 2020. Outgoing near-infrared radiation from vegetation scales with canopy photosynthesis across a Spectrum of function, structure, physiological capacity, and weather. Journal of geophysical research. Biogeosciences 125, e2019JG005534. https://doi.org/10.1029/2019JG005534.

Béland, M., Baldocchi, D., 2020. Is foliage clumping an outcome of resource limitations within forests? Agric. For. Meteorol. 295, 108185. https://doi.org/10.1016/j.agrformet.2020.108185.

Calders, K., Adams, J., Armston, J., Bartholomeus, H., Bauwens, S., Bentley, L.P., Chave, J., Danson, F.M., Demol, M., Disney, M., Gaulton, R., Krishna Moorthy, S.M., Levick, S.R., Saarinen, N., Schaaf, C., Stovall, A., Terryn, L., Wilkes, P., Verbeeck, H., 2020. Terrestrial laser scanning in forest ecology: expanding the horizon. Remote Sens. Environ. 251, 112102. https://doi.org/10.1016/j.rse.2020.112102.

Chang, C.Y., Guanter, L., Frankenberg, C., Köhler, P., Gu, L., Magney, T.S., Grossmann, K., Sun, Y., 2020. Systematic assessment of retrieval methods for canopy far-red solar-induced chlorophyll fluorescence using high-frequency automated Field spectroscopy. Journal of geophysical research. Biogeosciences 125, e2019JG005533. https://doi.org/10.1029/2019JG005533.

Chapin, F.S., 1980. The mineral nutrition of wild plants. Annu. Rev. Ecol. Syst. 11, 233–260. https://doi.org/10.1146/annurev.es.11.110180.001313.

Chianucci, F., Pisek, J., Raabe, K., Marchino, L., Ferrara, C., Corona, P., 2018. A dataset of leaf inclination angles for temperate and boreal broadleaf woody species. Ann. For. Sci. 75, 1–7. https://doi.org/10.1007/s13595-018-0730-x.

Christ, B., Hörtensteiner, S., 2014. Mechanism and significance of chlorophyll breakdown. J. Plant Growth Regul. 33, 4–20. https://doi.org/10.1007/s00344-013-9392-y.

Close, D.C., Beadle, C.L., 2006. Leaf angle responds to nitrogen supply in eucalypt seedlings. Is it a photoprotective mechanism? Tree Physiol. 26, 743–748. https://doi.org/10.1093/treephys/26.6.743.

Colwell, J.E., 1974. Vegetation canopy reflectance. Remote Sens. Environ. 3, 175–183. https://doi.org/10.1016/0034-4257(74)90003-0.

Croft, H., Chen, J.M., Luo, X., Bartlett, P., Chen, B., Staebler, R.M., 2017. Leaf chlorophyll content as a proxy for leaf photosynthetic capacity. Glob. Chang. Biol. 23, 3513–3524. https://doi.org/10.1111/gcb.13599.

Damm, A., Cogliati, S., Colombo, R., Fritsche, L., Genangeli, A., Genesio, L., Hanus, J., Peressotti, A., Rademske, P., Rascher, U., Schuettemeyer, D., Siegmann, B., Sturm, J., Miglietta, F., 2022. Response times of remote sensing measured sun-induced chlorophyll fluorescence, surface temperature and vegetation indices to evolving soil water limitation in a crop canopy. Remote Sens. Environ. 273, 112957. https://doi.org/10.1016/j.rse.2022.112957.

Dechant, B., Ryu, Y., Badgley, G., Zeng, Y., Berry, J.A., Zhang, Y., Goulas, Y., Li, Z., Zhang, Q., Kang, M., Li, J., Moya, I., 2020. Canopy structure explains the relationship between photosynthesis and sun-induced chlorophyll fluorescence in crops. Remote Sens. Environ. 241, 111733. https://doi.org/10.1016/j.rse.2020.111733.

Dechant, B., Ryu, Y., Badgley, G., Köhler, P., Rascher, U., Migliavacca, M., Zhang, Y., Tagliabue, G., Guan, K., Rossini, M., Goulas, Y., Zeng, Y., Frankenberg, C., Berry, J. A., 2022. NIRVP: a robust structural proxy for sun-induced chlorophyll fluorescence and photosynthesis across scales. Remote Sens. Environ. 268, 112763. https://doi.org/10.1016/j.rse.2021.112763.

Disney, M., 2019. Terrestrial LiDAR: a three-dimensional revolution in how we look at trees. New Phytol. 222, 1736–1741. https://doi.org/10.1111/nph.15517.

Du, S., Liu, X., Chen, J., Duan, W., Liu, L., 2023. Addressing validation challenges for TROPOMI solar-induced chlorophyll fluorescence products using tower-based measurements and an NIRv-scaled approach. Remote Sens. Environ. 290, 113547. https://doi.org/10.1016/j.rse.2023.113547.

Ellsworth, D.S., Reich, P.B., 1993. Canopy structure and vertical patterns of photosynthesis and related leaf traits in a deciduous forest. Oecologia 96, 169–178. https://doi.org/10.1007/BF00317729.

Féret, J.-B., Gitelson, A.A., Noble, S.D., Jacquemoud, S., 2017. PROSPECT-D: towards modeling leaf optical properties through a complete lifecycle. Remote Sens. Environ. 193, 204–215. https://doi.org/10.1016/j.rse.2017.03.004.

Field, C.B., 1991. 2 - ecological scaling of carbon gain to stress and resource availability. In: Mooney, H.A., Winner, W.E., Pell, E.J. (Eds.), Response of Plants to Multiple Stresses. Pergamon Programmed Texts. Academic Press, San Diego, pp. 35–65. https://doi.org/10.1016/B978-0-08-092483-0.50007-4.

Frankenberg, C., Berry, J., 2018. 3.10 - solar induced chlorophyll fluorescence: Origins, relation to photosynthesis and retrieval. In: Liang, S. (Ed.), Comprehensive Remote Sensing. Elsevier, Oxford, pp. 143–162. https://doi.org/10.1016/B978-0-12-409548-9.10632-3.

Frankenberg, C., Fisher, J.B., Worden, J., Badgley, G., Saatchi, S.S., Lee, J.-E., Toon, G.C., Butz, A., Jung, M., Kuze, A., Yokota, T., 2011. New global observations of the terrestrial carbon cycle from GOSAT: patterns of plant fluorescence with gross primary productivity. Geophys. Res. Lett. 38. https://doi.org/10.1029/2011GL048738.

Gamon, J.A., Field, C.B., Goulden, M.L., Griffin, K.L., Hartley, A.E., Joel, G., Penuelas, J., Valentini, R., 1995. Relationships between NDVI, canopy structure, and photosynthesis in three Californian vegetation types. Ecol. Appl. 5, 28–41. https://doi.org/10.2307/1942049.

Gamon, J.A., Huemmrich, K.F., Wong, C.Y.S., Ensminger, I., Garrity, S., Hollinger, D.Y., Noormets, A., Peñuelas, J., 2016. A remotely sensed pigment index reveals photosynthetic phenology in evergreen conifers. Proc. Natl. Acad. Sci. 113, 13087–13092. https://doi.org/10.1073/pnas.1606162113.

Gamon, J.A., Somers, B., Malenovský, Z., Middleton, E.M., Rascher, U., Schaepman, M. E., 2019. Assessing vegetation function with imaging spectroscopy. Surv. Geophys. 40, 489–513. https://doi.org/10.1007/s10712-019-09511-5.

Gastellu-Etchegorry, J.-P., Lauret, N., Yin, T., Landier, L., Kallel, A., Malenovský, Z., Bitar, A.A., Aval, J., Benhmida, S., Qi, J., Medjdoub, G., Guilleux, J., Chavanon, E., Cook, B., Morton, D., Chrysoulakis, N., Mitraka, Z., 2017. DART: recent advances in remote sensing data modeling with atmosphere, polarization, and chlorophyll fluorescence. IEEE J. Select. Top. Appl. Earth Observ. Remote Sens. 10, 2640–2649. https://doi.org/10.1109/JSTARS.2017.2685528.

Gates, D.M., Keegan, H.J., Schleter, J.C., Weidner, V.R., 1965. Spectral properties of plants. Appl. Opt, 4, 11–20. https://doi.org/10.1364/AO.4.000011.

Gitelson, A.A., Merzlyak, M.N., 1997. Remote estimation of chlorophyll content in higher plant leaves. Int. J. Remote Sens. 18, 2691–2697. https://doi.org/10.1080/014311697217558.

Givnish, T.J., 2020. The adaptive geometry of trees revisited. Am. Nat. 195, 935–947. https://doi.org/10.1086/708498.

Goel, N.S., Strebel, D.E., 1984. Simple Beta distribution representation of leaf orientation in vegetation Canopies1. Agron. J. 76, 800–802. https://doi.org/10.2134/agronj1984.00021962007600050021x.

Grime, J.P., 1977. Evidence for the existence of three primary strategies in plants and its relevance to ecological and evolutionary theory. Am. Nat. 111, 1169–1194.

Gu, L., Han, J., Wood, J.D., Chang, C.Y.-Y., Sun, Y., 2019. Sun-induced Chl fluorescence and its importance for biophysical modeling of photosynthesis based on light reactions. New Phytol. 223, 1179–1191. https://doi.org/10.1111/nph.15796.

Guillén-Escribà, C., Schneider, F.D., Schmid, B., Tedder, A., Morsdorf, F., Furrer, R., Hueni, A., Niklaus, P.A., Schaepman, M.E., 2021. Remotely sensed between-individual functional trait variation in a temperate forest. Ecol. Evol. 11, 10834–10867. https://doi.org/10.1002/ece3.7758.

Hase, N., Doktor, D., Rebmann, C., Dechant, B., Mollenhauer, H., Cuntz, M., 2022. Identifying the main drivers of the seasonal decline of near-infrared reflectance of a temperate deciduous forest. Agric. For. Meteorol. 313, 108746. https://doi.org/10.1016/j.agrformet.2021.108746.

Helm, L.T., Shi, H., Lerdau, M.T., Yang, X., 2020. Solar-induced chlorophyll fluorescence and short-term photosynthetic response to drought. Ecol. Appl. 30, e02101. https://doi.org/10.1002/eap.2101.

Hirose, T., 2005. Development of the Monsi–Saeki theory on canopy structure and function. Ann. Bot. 95, 483–494. https://doi.org/10.1093/aob/mci047.

Hirtreiter, J.N., Potts, D.L., 2012. Canopy structure, photosynthetic capacity and nitrogen distribution in adjacent mixed and monospecific stands of *Phragmites australis* and *Typha latifolia*. Plant Ecol. 213, 821–829. https://doi.org/10.1007/s11258-012-0044-2.

Horn, H.S., 1971. The Adaptive Geometry of Trees. Princeton University Press, Princeton, NJ.

Hörtensteiner, S., Feller, U., 2002. Nitrogen metabolism and remobilization during senescence. J. Exp. Bot. 53, 927–937. https://doi.org/10.1093/jexbot/53.370.927.

Hosoi, F., Omasa, K., 2006. Voxel-based 3-D modeling of individual trees for estimating leaf area density using high-resolution portable scanning Lidar. IEEE Trans. Geosci. Remote Sens. 44, 3610–3618. https://doi.org/10.1109/TGRS.2006.881743.

Jacquemoud, S., Verhoef, W., Baret, F., Bacour, C., Zarco-Tejada, P.J., Asner, G.P., François, C., Ustin, S.L., 2009. PROSPECT+SAIL models: a review of use for vegetation characterization. Remote Sens. Environ. Imaging Spectrosc. Spec. Issue 113, S56–S66. https://doi.org/10.1016/j.rse.2008.01.026.

Jia, M., Colombo, R., Rossini, M., Celesti, M., Zhu, J., Cogliati, S., Cheng, T., Tian, Y., Zhu, Y., Cao, W., Yao, X., 2021. Estimation of leaf nitrogen content and photosynthetic nitrogen use efficiency in wheat using sun-induced chlorophyll fluorescence at the leaf and canopy scales. Eur. J. Agron. 122, 126192. https://doi.org/10.1016/j.eja.2020.126192.

Johnson, J.E., Berry, J.A., 2021. The role of cytochrome b6f in the control of steady-state photosynthesis: a conceptual and quantitative model. Photosynth. Res. 148, 101–136. https://doi.org/10.1007/s11120-021-00840-4.

Jordan, C.F., 1969. Derivation of leaf-area index from quality of light on the Forest floor. Ecology 50, 663–666. https://doi.org/10.2307/1936256.

Jupp, D.L.B., Culvenor, D.S., Lovell, J.L., Newnham, G.J., Strahler, A.H., Woodcock, C.E., 2009. Estimating forest LAI profiles and structural parameters using a ground-based laser called 'Echidna®☆. Tree Physiol. 29, 171–181. https://doi.org/10.1093/treephys/tpn022.

Kattenborn, T., Richter, R., Guimarães-Steinicke, C., Feilhauer, H., Wirth, C., 2022. AngleCam: predicting the temporal variation of leaf angle distributions from image series with deep learning. Methods Ecol. Evol. 13, 2531–2545. https://doi.org/10.1111/2041-210X.13968.

Kattenborn, T., Wieneke, S., Montero, D., Mahecha, M.D., Richter, R., Guimarães-Steinicke, C., Wirth, C., Ferlian, O., Feilhauer, H., Sachsenmaier, L., Eisenhauer, N., Dechant, B., 2024. Temporal dynamics in vertical leaf angles can confound vegetation indices widely used in earth observations. Commun. Earth Environ. 5, 1–11. https://doi.org/10.1038/s43247-024-01712-0.

Kattge, J., Knorr, W., Raddatz, T., Wirth, C., 2009. Quantifying photosynthetic capacity and its relationship to leaf nitrogen content for global-scale terrestrial biosphere models. Glob. Chang. Biol. 15, 976–991. https://doi.org/10.1111/j.1365-2486.2008.01744.x.

Killingbeck, K.T., 1996. Nutrients in senesced leaves: keys to the search for potential resorption and resorption proficiency. Ecology 77, 1716–1727. https://doi.org/10.2307/2265777.

Kim, J., Ryu, Y., Dechant, B., Lee, H., Kim, H.S., Kornfeld, A., Berry, J.A., 2021. Solar-induced chlorophyll fluorescence is non-linearly related to canopy photosynthesis in a temperate evergreen needleleaf forest during the fall transition. Remote Sens. Environ. 258, 112362. https://doi.org/10.1016/j.rse.2021.112362.

Kimm, H., Guan, K., Jiang, C., Miao, G., Wu, G., Suyker, A.E., Ainsworth, E.A., Bernacchi, C.J., Montes, C.M., Berry, J.A., Yang, X., Frankenberg, C., Chen, M., Köhler, P., 2021. A physiological signal derived from sun-induced chlorophyll fluorescence quantifies crop physiological response to environmental stresses in the U.S. Corn Belt. Environ. Res. Lett. 16, 124051. https://doi.org/10.1088/1748-9326/ac3b16.

Knyazikhin, Y., Schull, M.A., Stenberg, P., Mõttus, M., Rautiainen, M., Yang, Y., Marshak, A., Latorre Carmona, P., Kaufmann, R.K., Lewis, P., Disney, M.I., Vanderbilt, V., Davis, A.B., Baret, F., Jacquemoud, S., Lyapustin, A., Myneni, R.B., 2013. Hyperspectral remote sensing of foliar nitrogen content. Proc. Natl. Acad. Sci. 110, E185–E192. https://doi.org/10.1073/pnas.1210196109.

Koffi, E.N., Rayner, P.J., Norton, A.J., Frankenberg, C., Scholze, M., 2015. Investigating the usefulness of satellite-derived fluorescence data in inferring gross primary productivity within the carbon cycle data assimilation system. Biogeosciences 12, 4067–4084. https://doi.org/10.5194/bg-12-4067-2015.

Kuai, B., Chen, J., Hörtensteiner, S., 2018. The biochemistry and molecular biology of chlorophyll breakdown. J. Exp. Bot. 69, 751–767. https://doi.org/10.1093/jxb/erx322.

Li, S., Dai, L., Wang, H., Wang, Y., He, Z., Lin, S., 2017. Estimating leaf area density of individual trees using the point cloud segmentation of terrestrial LiDAR data and a voxel-based model. Remote Sens 9, 1202. https://doi.org/10.3390/rs9111202.

Li, X., Xiao, J.F., He, B.B., Arain, M.A., Beringer, J., Desai, A.R., Emmel, C., Hollinger, D. Y., Krasnova, A., Mammarella, I., Noe, S.M., Ortiz, P.S., Rey-Sanchez, A.C., Rocha, A. V., Varlagin, A., 2018. Solar-induced chlorophyll fluorescence is strongly correlated with terrestrial photosynthesis for a wide variety of biomes: first global analysis based on OCO-2 and flux tower observations. Glob. Chang. Biol. 24, 3990–4008. https://doi.org/10.1111/gcb.14297.

Lusk, C.H., Wright, I., Reich, P.B., 2003. Photosynthetic differences contribute to competitive advantage of evergreen angiosperm trees over evergreen conifers in productive habitats. New Phytol. 160, 329–336. https://doi.org/10.1046/j.1469-8137.2003.00879.x.

Ma, L., Zheng, G., Wang, X., Li, S., Lin, Y., Ju, W., 2018. Retrieving forest canopy clumping index using terrestrial laser scanning data. Remote Sens. Environ. 210, 452–472. https://doi.org/10.1016/j.rse.2018.03.034.

Magney, T.S., Barnes, M.L., Yang, X., 2020. On the covariation of chlorophyll fluorescence and photosynthesis across scales. Geophys. Res. Lett. 47, e2020GL091098. https://doi.org/10.1029/2020GL091098.

Maguire, A.J., Eitel, J.U.H., Magney, T.S., Frankenberg, C., Köhler, P., Orcutt, E.L., Parazoo, N.C., Pavlick, R., Pierrat, Z.A., 2021. Spatial covariation between solar-induced fluorescence and vegetation indices from Arctic-boreal landscapes. Environ. Res. Lett. 16, 095002. https://doi.org/10.1088/1748-9326/ac188a.

Marrs, J.K., Reblin, J.S., Logan, B.A., Allen, D.W., Reinmann, A.B., Bombard, D.M., Tabachnik, D., Hutyra, L.R., 2020. Solar-induced fluorescence does not track photosynthetic carbon assimilation following induced stomatal closure. Geophys. Res. Lett. 47, e2020GL087956. https://doi.org/10.1029/2020GL087956.

Martini, D., Sakowska, K., Wohlfahrt, G., Pacheco-Labrador, J., van der Tol, C., Porcar-Castell, A., Magney, T.S., Carrara, A., Colombo, R., El-Madany, T.S., Gonzalez-Cascon, R., Martín, M.P., Julitta, T., Moreno, G., Rascher, U., Reichstein, M., Rossini, M., Migliavacca, M., 2022. Heatwave breaks down the linearity between sun-induced fluorescence and gross primary production. New Phytol. 233, 2415–2428. https://doi.org/10.1111/nph.17920.

McConnaughay, K.D.M., Bassow, S.L., Berntson, G.M., Bazzaz, F.A., 1996. Leaf senescence and decline of end-of-season gas exchange in five temperate deciduous tree species grown in elevated CO2 concentrations. Glob. Chang. Biol. 2, 25–33. https://doi.org/10.1111/j.1365-2486.1996.tb00046.x.

McNeil, B.E., Fahey, R.T., King, C.J., Erazo, D.A., Heimerl, T.Z., Elmore, A.J., 2023. Tree crown economics. Front. Ecol. Environ. 21, 40–48. https://doi.org/10.1002/fee.2588.

Meroni, M., Busetto, L., Colombo, R., Guanter, L., Moreno, J., Verhoef, W., 2010. Performance of spectral fitting methods for vegetation fluorescence quantification. Remote Sens. Environ. 114, 363–374. https://doi.org/10.1016/j.rse.2009.09.010.

Migliavacca, M., Perez-Priego, O., Rossini, M., El-Madany, T.S., Moreno, G., Tol, C. van der, Rascher, U., Berninger, A., Bessenbacher, V., Burkart, A., Carrara, A., Fava, F., Guan, J.-H., Hammer, T.W., Henkel, K., Juarez-Alcalde, E., Julitta, T., Kolle, O., Martín, M.P., Musavi, T., Pacheco-Labrador, J., Pérez-Burgueño, A., Wutzler, T., Zaehle, S., Reichstein, M., 2017. Plant functional traits and canopy structure control the relationship between photosynthetic CO2 uptake and far-red sun-induced fluorescence in a Mediterranean grassland under different nutrient availability. New Phytol. 214, 1078–1091. https://doi.org/10.1111/nph.14437.

Monsi, M., Saeki, T., 1953. Uber den Lichtfaktor in den Pflanzengesellschaften und seine Bedeutung fur die Stoffproduktion. Jpn. J. Bot. 14, 22–52.

Mooney, H.A., Gulmon, S.L., 1979. Environmental and evolutionary constraints on the photosynthetic characteristics of higher plants. In: Solbrig, O.T., Jain, S., Johnson, G. B., Raven, P.H. (Eds.), Topics in Plant Population Biology. Macmillan Education UK, London, pp. 316–337. https://doi.org/10.1007/978-1-349-04627-0_14.

Myneni, R.B., Ross, J. (Eds.), 1991. Photon-Vegetation Interactions: Applications in Optical Remote Sensing and Plant Ecology. Springer, Berlin, Heidelberg. https://doi.org/10.1007/978-3-642-75389-3.

Nakagawa, S., Johnson, P.C.D., Schielzeth, H., 2017. The coefficient of determination R2 and intra-class correlation coefficient from generalized linear mixed-effects models revisited and expanded. J. R. Soc. Interface 14, 20170213. https://doi.org/10.1098/rsif.2017.0213.

Niinemets, Ü., 2010. A review of light interception in plant stands from leaf to canopy in different plant functional types and in species with varying shade tolerance. Ecol. Res. 25, 693–714. https://doi.org/10.1007/s11284-010-0712-4.

Nilson, T., 1971. A theoretical analysis of the frequency of gaps in plant stands. Agric. Meteorol. 8, 25–38. https://doi.org/10.1016/0002-1571(71)90092-6.

Ollinger, S.V., 2011. Sources of variability in canopy reflectance and the convergent properties of plants. New Phytol. 189, 375–394. https://doi.org/10.1111/j.1469-8137.2010.03536.x.

Pierrat, Z., Nehemy, M.F., Roy, A., Magney, T., Parazoo, N.C., Laroque, C., Pappas, C., Sonnentag, O., Grossmann, K., Bowling, D.R., Seibt, U., Ramirez, A., Johnson, B., Helgason, W., Barr, A., Stutz, J., 2021. Tower-based remote sensing reveals mechanisms behind a two-phased spring transition in a mixed-species boreal Forest. J. Geophys. Res. Biogeosci. 126, e2020JG006191. https://doi.org/10.1029/2020JG006191.

Pierrat, Z., Magney, T., Parazoo, N.C., Grossmann, K., Bowling, D.R., Seibt, U., Johnson, B., Helgason, W., Barr, A., Bortnik, J., Norton, A., Maguire, A., Frankenberg, C., Stutz, J., 2022. Diurnal and seasonal dynamics of solar-induced chlorophyll fluorescence, vegetation indices, and gross primary productivity in the boreal Forest. Journal of geophysical research. Biogeosciences 127, e2021JG006588. https://doi.org/10.1029/2021JG006588.

Pisek, J., Diaz-Pines, E., Matteucci, G., Noe, S., Rebmann, C., 2022. On the leaf inclination angle distribution as a plant trait for the most abundant broadleaf tree species in Europe. Agric. For. Meteorol. 323, 109030. https://doi.org/10.1016/j.agrformet.2022.109030.

Porcar-Castell, A., Tyystjärvi, E., Atherton, J., van der Tol, C., Flexas, J., Pfündel, E.E., Moreno, J., Frankenberg, C., Berry, J.A., 2014. Linking chlorophyll a fluorescence to photosynthesis for remote sensing applications: mechanisms and challenges. J. Exp. Bot. 65, 4065–4095. https://doi.org/10.1093/jxb/eru191.

Raabe, K., Pisek, J., Sonnentag, O., Annuk, K., 2015. Variations of leaf inclination angle distribution with height over the growing season and light exposure for eight broadleaf tree species. Agric. For. Meteorol. 214–215, 2–11. https://doi.org/10.1016/j.agrformet.2015.07.008.

Reich, P.B., 2014. The world-wide 'fast–slow' plant economics spectrum: a traits manifesto. J. Ecol. 102, 275–301. https://doi.org/10.1111/1365-2745.12211.

Running, S.W., Nemani, R.R., Heinsch, F.A., Zhao, M., Reeves, M., Hashimoto, H., 2004. A continuous satellite-derived measure of global terrestrial primary production. BioScience 54, 547–560. https://doi.org/10.1641/0006-3568(2004)054[0547:ACSMOG]2.0.CO;2.

Schraik, D., Wang, D., Hovi, A., Rautiainen, M., 2023. Quantifying stand-level clumping of boreal, hemiboreal and temperate European forest stands using terrestrial laser scanning. Agric. For. Meteorol. 339, 109564. https://doi.org/10.1016/j.agrformet.2023.109564.

Sellers, P.J., 1985. Canopy reflectance, photosynthesis and transpiration. Int. J. Remote Sens. 6, 1335–1372. https://doi.org/10.1080/01431168508948283.

Sellers, P.J., 1987. Canopy reflectance, photosynthesis, and transpiration, II. The role of biophysics in the linearity of their interdependence. Remote Sens. Environ. 21, 143–183. https://doi.org/10.1016/0034-4257(87)90051-4.

Serbin, S.P., Singh, A., McNeil, B.E., Kingdon, C.C., Townsend, P.A., 2014. Spectroscopic determination of leaf morphological and biochemical traits for northern temperate and boreal tree species. Ecol. Appl. 24, 1651–1669. https://doi.org/10.1890/13-2110.1.

Stovall, A.E.L., Masters, B., Fatoyinbo, L., Yang, X., 2021. TLSLeAF: automatic leaf angle estimates from single-scan terrestrial laser scanning. New Phytol. 232, 1876–1892. https://doi.org/10.1111/nph.17548.

Sun, Y., Frankenberg, C., Wood, J.D., Schimel, D.S., Jung, M., Guanter, L., Drewry, D.T., Verma, M., Porcar-Castell, A., Griffis, T.J., Gu, L., Magney, T.S., Kohler, P., Evans, B., Yuen, K., 2017. OCO-2 advances photosynthesis observation from space via solar-induced chlorophyll fluorescence. Science 358, 6. https://doi.org/10.1126/science.aam5747.

Sun, Y., Gu, L., Wen, J., van der Tol, C., Porcar-Castell, A., Joiner, J., Chang, C.Y., Magney, T., Wang, L., Hu, L., Rascher, U., Zarco-Tejada, P., Barrett, C.B., Lai, J., Han, J., Luo, Z., 2023a. From remotely sensed solar-induced chlorophyll fluorescence to ecosystem structure, function, and service: part I—harnessing theory. Glob. Chang. Biol. 29, 2926–2952. https://doi.org/10.1111/gcb.16634.

Sun, Y., Wen, J., Gu, L., Joiner, J., Chang, C.Y., van der Tol, C., Porcar-Castell, A., Magney, T., Wang, L., Hu, L., Rascher, U., Zarco-Tejada, P., Barrett, C.B., Lai, J., Han, J., Luo, Z., 2023b. From remotely-sensed solar-induced chlorophyll fluorescence to ecosystem structure, function, and service: part II—harnessing data. Glob. Chang. Biol. 29, 2893–2925. https://doi.org/10.1111/gcb.16646.

Townsend, P.A., Serbin, S.P., Kruger, E.L., Gamon, J.A., 2013. Disentangling the contribution of biological and physical properties of leaves and canopies in imaging spectroscopy data. Proc. Natl. Acad. Sci. USA 110, E1074. https://doi.org/10.1073/pnas.1300952110.

Tubuxin, B., Rahimzadeh-Bajgiran, P., Ginnan, Y., Hosoi, F., Omasa, K., 2015. Estimating chlorophyll content and photochemical yield of photosystem II (ΦPSII) using solar-induced chlorophyll fluorescence measurements at different growing stages of attached leaves. J. Exp. Bot. 66, 5595–5603. https://doi.org/10.1093/jxb/erv272.

Tucker, C.J., 1979. Red and photographic infrared linear combinations for monitoring vegetation. Remote Sens. Environ. 8, 127–150. https://doi.org/10.1016/0034-4257(79)90013-0.

van der Tol, C., Verhoef, W., Timmermans, J., Verhoef, A., Su, Z., 2009. An integrated model of soil-canopy spectral radiances, photosynthesis, fluorescence, temperature and energy balance. Biogeosciences 6, 3109–3129.

van der Tol, C., Berry, J.A., Campbell, P.K.E., Rascher, U., 2014. Models of fluorescence and photosynthesis for interpreting measurements of solar-induced chlorophyll fluorescence. J. Geophys. Res.Biogeosci. 119, 2312–2327. https://doi.org/10.1002/2014jg002713.

Verhoef, W., 1997. Theory of Radiative Transfer Models Applied in Optical Remote Sensing of Vegetation Canopies. Wageningen Agricultural University.

Verrelst, J., van der Tol, C., Magnani, F., Sabater, N., Rivera, J.P., Mohammed, G., Moreno, J., 2016. Evaluating the predictive power of sun-induced chlorophyll fluorescence to estimate net photosynthesis of vegetation canopies: a SCOPE modeling study. Remote Sens. Environ. 176, 139–151. https://doi.org/10.1016/j.rse.2016.01.018.

Vicari, M.B., Pisek, J., Disney, M., 2019. New estimates of leaf angle distribution from terrestrial LiDAR: comparison with measured and modelled estimates from nine broadleaf tree species. Agric. For. Meteorol. 264, 322–333. https://doi.org/10.1016/j.agrformet.2018.10.021.

Wang, N., Clevers, J.G.P.W., Wieneke, S., Bartholomeus, H., Kooistra, L., 2022. Potential of UAV-based sun-induced chlorophyll fluorescence to detect water stress in sugar beet. Agric. For. Meteorol. 323, 109033. https://doi.org/10.1016/j.agrformet.2022.109033.

Weng, X.-Y., Xu, H.-X., Jiang, D.-A., 2005. Characteristics of gas exchange, chlorophyll fluorescence and expression of key enzymes in photosynthesis during leaf senescence in Rice plants. J. Integr. Plant Biol. 47, 560–566. https://doi.org/10.1111/j.1744-7909.2005.00098.x.

Wieneke, S., Burkart, A., Cendrero-Mateo, M.P., Julitta, T., Rossini, M., Schickling, A., Schmidt, M., Rascher, U., 2018. Linking photosynthesis and sun-induced fluorescence at sub-daily to seasonal scales. Remote Sens. Environ. 219, 247–258. https://doi.org/10.1016/j.rse.2018.10.019.

Wong, C.Y.S., D'Odorico, P., Arain, M.A., Ensminger, I., 2020. Tracking the phenology of photosynthesis using carotenoid-sensitive and near-infrared reflectance vegetation indices in a temperate evergreen and mixed deciduous forest. New Phytol. 226, 1682–1695. https://doi.org/10.1111/nph.16479.

Wu, L., Zhang, X., Rossini, M., Wu, Y., Zhang, Z., Zhang, Y., 2022. Physiological dynamics dominate the response of canopy far-red solar-induced fluorescence to herbicide treatment. Agric. For. Meteorol. 323, 109063. https://doi.org/10.1016/j.agrformet.2022.109063.

Yang, X., Tang, J.W., Mustard, J.F., Lee, J.E., Rossini, M., Joiner, J., Munger, J.W., Kornfeld, A., Richardson, A.D., 2015. Solar-induced chlorophyll fluorescence that correlates with canopy photosynthesis on diurnal and seasonal scales in a temperate deciduous forest. Geophys. Res. Lett. 42, 2977–2987. https://doi.org/10.1002/2015gl063201.

Yang, K., Ryu, Y., Dechant, B., Berry, J.A., Hwang, Y., Jiang, C., Kang, M., Min, J., Kimm, H., Kornfeld, A., Yang, X., 2018a. Sun-induced chlorophyll fluorescence is more strongly related to absorbed light than to photosynthesis at half-hourly resolution in a rice paddy. Remote Sens. Environ. 216, 658–673. https://doi.org/10.1016/j.rse.2018.07.008.

Yang, X., Shi, H., Stovall, A., Guan, K., Miao, G., Zhang, Yongguang, Zhang, Yao, Xiao, X., Ryu, Y., Lee, J.-E., 2018b. FluoSpec 2—an automated Field spectroscopy system to monitor canopy solar-induced fluorescence. Sensors 18, 2063. https://doi.org/10.3390/s18072063.

Yang, X., Li, R., Jablonski, A., Stovall, A., Kim, J., Yi, K., Ma, Y., Beverly, D., Phillips, R., Novick, K., Xu, X., Lerdau, M., 2023. Leaf angle as a leaf and canopy trait:

rejuvenating its role in ecology with new technology. Ecol. Lett. 26, 1005–1020. https://doi.org/10.1111/ele.14215.

Zeng, Y., Badgley, G., Dechant, B., Ryu, Y., Chen, M., Berry, J.A., 2019. A practical approach for estimating the escape ratio of near-infrared solar-induced chlorophyll fluorescence. Remote Sens. Environ. 232, 111209. https://doi.org/10.1016/j.rse.2019.05.028.

Zeng, Y., Chen, M., Hao, D., Damm, A., Badgley, G., Rascher, U., Johnson, J.E., Dechant, B., Siegmann, B., Ryu, Y., Qiu, H., Krieger, V., Panigada, C., Celesti, M., Miglietta, F., Yang, X., Berry, J.A., 2022. Combining near-infrared radiance of vegetation and fluorescence spectroscopy to detect effects of abiotic changes and stresses. Remote Sens. Environ. 270, 112856. https://doi.org/10.1016/j.rse.2021.112856.

Zhang, Y., Guanter, L., Berry, J.A., Joiner, J., van der Tol, C., Huete, A., Gitelson, A., Voigt, M., Köhler, P., 2014. Estimation of vegetation photosynthetic capacity from space-based measurements of chlorophyll fluorescence for terrestrial biosphere models. Glob. Chang. Biol. 20, 3727–3742. https://doi.org/10.1111/gcb.12664.